

Observations of spatial and velocity structure in the Orion Molecular Cloud*

H. D. Nissen¹, M. Gustafsson¹, J.L. Lemaire^{2, **}, Y. Clénet³, D. Rouan³, and D. Field^{1, **}

¹ Department of Physics and Astronomy, University of Aarhus, 8000 Aarhus C, Denmark

² Observatoire de Paris and Université de Cergy-Pontoise, LERMA and UMR 8112 du CNRS, 92195 Meudon, France

³ Observatoire de Paris-Meudon, LESIA, 92195 Meudon Principal Cedex, France

Received 2nd December 2024/ Accepted 2nd December 2024

Abstract Observations are reported of H₂ IR emission in the S(1) v=1-0 line at 2.121 μ m in the Orion Molecular Cloud, OMC1, using the GriF instrument on the Canada-France-Hawaii Telescope. GriF uses a combination of adaptive optics and Fabry-Perot interferometry, yielding a spatial resolution of 0.15'' to 0.18'' and a velocity discrimination as high as 1 km s⁻¹. Thanks to the high spatial and velocity resolution of the GriF data, 193 bright H₂ emission regions can be identified in OMC1. The general characteristics of these features are described in terms of radial velocities, brightness and spatial displacement of maxima of velocity and brightness, the latter to yield the orientation of flows in the plane of the sky. Strong spatial correlation between velocity and bright H₂ emission is found and serves to identify many features as shocks. Important results are: (i) velocities of the excited gas illustrate the presence of a zone to the south of BN-IRc2 and Peak 1, and the west of Peak 2, where there is a powerful blue-shifted outflow with an average velocity of -18 km s⁻¹. This is shown to be the NIR counterpart of an outflow identified in the radio from source I, a very young O-star. (ii) There is a band of weak velocity features (<5 km s⁻¹) in Peak 1 which may share a common origin through an explosive event, in the BN-IRc2 region, with the fast-moving fingers (or bullets) to the NW of OMC1. (iii) A proportion of the flows are likely to represent sites of low mass star formation and several regions show multiple outflows, probably indicative of multiple star formation within OMC1. The high spatial and velocity resolution of the GriF data show these and other features in more detail than has previously been possible.

Key words. ISM: individual objects: OMC1, source I – ISM: kinematics and dynamics – ISM: molecules – shocks waves

1. Introduction

The Orion Molecular Cloud (OMC1) (D = 460 pc, Bally et al. 2000) is the closest highly active massive star-forming region. It has accordingly been studied over a large range of wavelengths from the radio to the X-ray (e.g. Genzel & Stutzki 1989; Wright et al. 1996; O'Dell 2001; Chrysostomou et al. 2000; Garmire et al. 2000; Ferland 2001; Feigelson et al. 2002; Doi et al. 2002; O'Dell & Doi 2003; Tan 2004) and has become the type-site for studies of star formation. Many features are accordingly very well-described, for example the detailed morphology of the HII region associated with θ^1 Ori C, the dominant source of ionizing radiation in the Trapezium (O'Dell 2001). Perhaps the principal significance of OMC1 and its

vicinity is that it has been shown to harbour upward of 1000 young low mass stars in the presence of a number of high mass stars (Hillenbrand 1997).

The present work, covering the area shown in Figs. 1 and 2, concentrates upon infrared observations of molecular hydrogen (H₂), and in particular upon data displaying the dynamics of OMC1. The gas in OMC1 is highly structured with many bright knots and there is ample evidence of much violent motion within OMC1 over a range of scales from 70 AU to 3 x 10⁴ AU (Gustafsson et al. 2006). Earlier work concerning gas dynamics (Chrysostomou et al. 1997; Salas et al. 1999; Gustafsson et al. 2003) showed the presence of numerous gas flows with flow velocities varying from a few km s⁻¹ in relatively dense gas to several hundred km s⁻¹ (Lee & Burton 2000; Doi et al. 2002). The latter are associated with perhaps the most prominent feature in OMC1, the H₂ "fingers" (also known as "bullets") first observed by Allen & Burton (1993). The fingers lie principally to the

Send offprint requests to: D. Field, e-mail: dfield@phys.au.dk

* Based on observations performed at the CFHT 3.6 m telescope

** Visiting astronomer at the Canada-France-Hawaii Telescope, Mauna Kea, Hawaii

NW of OMC1 and they are the wake of fast-moving, diffuse clumps of gas moving radially out from OMC1 (Burton 1997; Lee & Burton 2000; Doi et al. 2002). We do not find any high velocity fingers in the observed field. This may be due to the limitations of the observations which confine us to velocities below about 150 km s^{-1} but may also be due to the technique of data reduction, as further described in sec. 2.

Two main categories of models have been proposed to explain the overall structure of OMC1. One is that structures in OMC1 are caused by shock instabilities which form the bright knots and bullets as in Stone et al. (1995) and McCaughrean & Mac Low (1997). In this model Rayleigh-Taylor instabilities form in the wind from the central massive star (or stars) in OMC1 when a faster wind overtakes the dense shell of material swept up by an earlier, slower wind. This results in a fragmentation of the shell into smaller knots some of which appears as bullets, forming fingers of emission, when moving outwards from the shell at high speed. The other group of models (e.g. Allen & Burton 1993; Doi et al. 2002) explain the bright knots as internal shocks in the cloud. These can have many origins: turbulent bipolar outflows from low-mass star formation or some form of outflow from the central massive stars (BN, source I, source n (Menten & Reid 1995; Greenhill et al. 2004a; Shuping et al. 2004)). The fingers and bullets themselves in either model are typically interpreted as the result of some major explosive event involving one or more of the massive stars. The fingers may then have shot through Peak 1 rather than being formed there. The lack of fingers and bullets to the SE of OMC1 could suggest a highly directional origin, but may equally well be explained by the emitting H_2 being too deeply buried to be seen, or it has been evaporated by the action of the Trapezium stars; if you placed the bullets to the NW in the corresponding position to the SE, they would have come very close to the Trapezium. For further discussion of the fingers and bullets we refer the reader to for example Axon & Taylor (1984); Allen & Burton (1993); Burton (1997); O'Dell et al. (1997); Lee & Burton (2000); O'Dell (2001); Doi et al. (2002).

In this work we would favour the second group of models mentioned above, in which a significant proportion of the excitation is internal to Peak 1 (see fig. 2 for nomenclature). We also note there are no prominent fingers in Peak 2 and therefore Peak 2 must presumably have some internal excitation source. In separate work we have also studied the global nature of the gas motions in OMC1 (Gustafsson et al. 2006). In that work a statistical analysis is presented of the turbulent velocity structure in the Orion Molecular Cloud at scales

ranging from 70 AU to 3×10^4 AU, using the data of the present paper. The variance for the velocity field shows only an approximate power law dependence on lag, with deviations below 2000 AU which are attributed to outflows and possibly disk structures, below 300 AU, associated with low mass star formation within OMC1. The major point is that the analysis in Gustafsson et al. (2006) demonstrates the presence of one or more preferred scales in the excited gas. These preferred scales are most naturally attributed to star formation where deviations from power law behaviour is associated with injection of energy at and below the star-forming scale.

Energy injection into OMC1 is evidently triggered within the molecular cloud at different scales. Massive stars such as the BN object, a B-star (Gezari et al. 1998), or radio source I (hereafter simply source I), a deeply buried O-star (Menten & Reid 1995; Greenhill et al. 2004a; Shuping et al. 2004), are associated with structure at a scale of ~ 0.1 pc (20,000 AU). Low mass star formation gives rise to flows and associated structure at scales of hundreds to several thousand AU.

The region studied in the present work is shown in Fig. 1 and lies NW of the Trapezium stars. The target area covers only the inner part of OMC1, and as we have noted largely excludes for example bullets and fingers. Thus the material in the present study encompasses the gas volume that tends to be subject to denser, slower outflows, associated with both massive star formation and low mass star formation.

High spatial resolution K-band (2-2.5 μm) images of IR emission from H_2 in OMC1 using the HST (Stolovy et al. 1998; Chen et al. 1998; Schultz et al. 1999; Doi et al. 2002), the Canada-France-Hawaii Telescope (CFHT) (Gustafsson et al. 2003), the ESO 3.6m (Vannier et al. 2001; Kristensen et al. 2003), the VLT (Lacombe et al. 2004) and other telescopes (e.g. McCaughrean & Mac Low 1997; Schild et al. 1997) have provided the most recent evidence for the presence of fast flows and shocks at small scales in OMC1.

The recent paper of Gustafsson et al. (2003), hereafter Paper I, provided an initial report of H_2 emission data for OMC1 obtained using the so-called "GriF" instrument (Clénet et al. 2002) on the CFHT in December 2000. This instrument combines Fabry-Perot interferometry with the PUEO adaptive optics system on the CFHT (Rigaut et al. 1998). These data, containing information on both morphology and velocity, showed striking evidence for the presence of shocks within OMC1. This was provided through the clear association of gas motions of tens of km s^{-1} with bright IR emission of H_2 . The novelty of these data is contained in the association of a very high spatial resolution of $0.15''$ (70 AU) to $0.18''$ with velocity discrimination as good as 1 km s^{-1} (3σ) in regions of high emission brightness, obtained with a Fabry-Perot of relatively low resolution of 150 km s^{-1} . These figures may be compared with the high inherent spectral resolution of

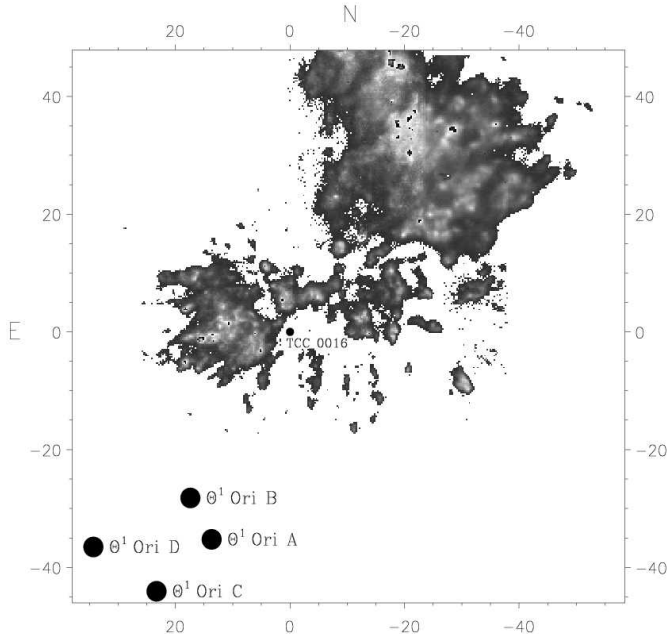


Figure 1. The observed area relative to the Trapezium stars (large black dots). The grey scale image show emission brightness in the H_2 $v=1-0$ $S(1)$ line. Axes are labelled in arcseconds. The star TCC0016, at coordinates $0''$ E, $0''$ N and marked with a small black dot, is used as a reference for coordinates throughout this work.

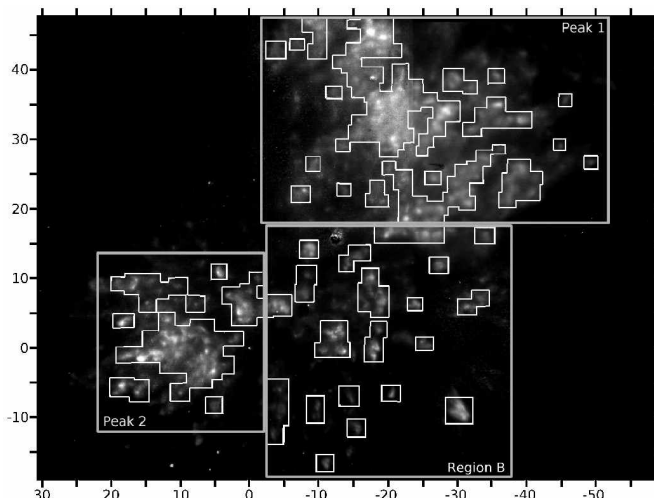


Figure 2. The regions analysed in this work outlined as small overlapping white boxes. The gray-scale shows emission in the H_2 $v=1-0$ $S(1)$ emission line. Also shown as large white boxes is the naming convention for Peak 1, Peak 2 (Beckwith et al. 1978), and Region B, the latter bounded by $-2''$ – $-40''$ E, $-18''$ – $-17''$ N, relative to TCC0016. Axes are labelled in arcseconds.

14 km s^{-1} in Chrysostomou et al. (1997) and 24 km s^{-1} in Salas et al. (1999), where data were recorded with a spatial resolution which lay between $1.5''$ and $2.0''$. In the present work the GriF data are reported in detail. Whereas in Paper I 19 regions were identified for study,

193 regions are included here. This affords a much broader perspective on the nature of flows within OMC1 and represents a detailed attempt at extracting the wealth of information contained within the GriF observations. New features are revealed through this extended study of the GriF results. In particular, a massive and very energetic blue-shifted outflow is identified in Region B between Peak 1 and Peak 2 (fig. 2). Chrysostomou et al. (1997), working in K-band at a spatial resolution of $1.5''$ found evidence of clumps of gas dominated by blue-shifted motions in the same zone. As described in sect. 6, there is a considerable independent body of evidence from radio data for an outflow in this zone (Genzel et al. 1981; Genzel & Stutzki 1989; Wright et al. 1996; Greenhill et al. 2004a; Doeleman et al. 2004). The outflow detected here in excited H_2 is characterised in some detail and it is shown that the outflow is the IR signature of the outflow identified through radio observations.

On a smaller scale, numerous regions of bright H_2 emission are identified in Peak 1, the NW region, which show only weak radial velocity components with no clear velocity structure. In addition there are several regions on the 1000 AU scale with multiple outflows. If, as we discuss in some detail here, there are protostars associated with some of these latter zones, then our data present a picture of star formation that is more complex than the simple disk-bipolar outflow model of single star formation.

In sect. 2 the observations and data reduction, described in detail in Paper I, are briefly reviewed. Sect. 3 illustrates and collates the data for all 193 regions in terms of radial velocities of flows, brightness of emission associated with these flows and the displacement in the plane of the sky between the maximum in emission brightness and the maximum in local radial velocity. The mechanism of H_2 excitation is also briefly discussed. In sect. 4, the data are presented in order to give a global view of the spatial distribution of radial flow velocities and the characteristics of various zones. Among major points that emerge are (i) the presence of the outflow mentioned above between Peaks 1 and 2, in Region B (Fig. 2), (ii) the accumulation of zones with high H_2 brightness but with $<5 \text{ km s}^{-1}$ radial motion in a region passing diagonally across Peak 1, (iii) the greater tendency for shocked regions to group more closely in Peak 2 than in Peak 1 and (iv) the fact that maxima in brightness of emission and in velocity are in general slightly displaced. In sect. 5 a short qualitative account of the structure of shocks is followed by the use of data to establish the orientations of shocks within the plane of the sky. Then follows a consideration of possible sites of current low mass star formation in OMC1. In sect. 6 the origin of the outflow in Region B and its spatial association with continuum sources in the IR and radio is discussed in detail.

2. Observations and data reduction

Observations were performed of the regions shown in Figs. 1 and 2 on December 5th 2000 at the 3.6m CFHT,

using the then new instrument GriF (Clénet et al. 2002). This instrument combines the high spatial resolution of the PUEO adaptive optics with spectral resolution provided by a Queensgate ET50WF Fabry-Perot interferometer (FP), giving a data-cube showing brightness in each position (pixel) for a series of wavelengths. The total observed region in OMC1 is a $\sim 1' \times 1'$ area centered approximately on the BN-object, as shown in Fig. 2.

Observations were made in the K-band using the H_2 $v=1-0$ S(1) emission line, which has a rest wavelength of $2.1212544 \mu\text{m}$ (Bragg et al. 1982). The line was scanned using the FP with a step size of $\sim 4.5 \times 10^{-4} \mu\text{m}$ to obtain images showing the brightness at a series of wavelengths on both sides of the rest wavelength. A H_2 $v=1-0$ S(1) interference filter of central wavelength $2.122 \mu\text{m}$ and bandwidth of $0.02 \mu\text{m}$ was inserted between the FP and the detector to prevent the superposition of different FP orders. The spatial resolution of the data was $0.15''$, estimated from the PSF of stars in the field. The pixel scale was $0.035''$. The inherent spectral resolution of the FP was 150 km s^{-1} . To reduce the level of noise, the data have been smoothed with a moving boxcar average over 3×3 pixels, resulting in a 20% loss of spatial resolution, that is, the final resolution of the data is $0.18''$. For a given position in the plane of the sky the data give the count rate for each observed wavelength. This is then fitted with a lorentzian (Clénet et al. 2002; Chrysostomou et al. 1997, and Paper I) to find the maximum count rate and the corresponding wavelength. This gives the velocity of the gas at that position. Due to high signal-to-noise very precise fits can be made. In bright regions the uncertainty in the fitted velocity is $\pm 1 \text{ km s}^{-1}$ or less at 3σ . In the dimmest regions examined in this work (with a very few exceptions) the uncertainty in the peak in the lorentzian, used to determine flow velocities (see sect. 3.1), is $\leq 2 \text{ km s}^{-1}$ while velocities of the gas surrounding regions of flow typically have uncertainties of $3-4 \text{ km s}^{-1}$. A detailed account of the errors associated with velocity determination may be found in Gustafsson et al. (2006) where the uncertainty associated with velocity determination and the counts per pixel per exposure are explicitly related through an empirical formula.

Where weaker high velocity emission is seen spatially coincident with stronger low velocity emission, we record only the velocity of the brighter slower gas. This is however a rare occurrence and we are aware of only two cases where this has been encountered: (i) the emission feature around position $-24.2''$ E $6.5''$ N where Stolovy et al. (1998) find a weak high velocity component together with the stronger low velocity feature which we find and (ii) at $-19.7''$ E $16.2''$ N where we observe the object HH208 at a radial velocity of -19 km s^{-1} . HH208 has however been identified as a bullet, on the basis of associated FeII emission, with a radial velocity between -120 and -180 km s^{-1} , Axon & Taylor (1984); O'Dell et al. (1997).

Velocity calibration was carried out by assigning to the mean velocity of all data a value of $12 \pm 6 \text{ km s}^{-1}$ in the local standard of rest (v_{lsr}), consistent with data in Chrysostomou et al. (1997); Salas et al. (1999) and O'Dell (2001). Velocity calibration is however not material to this work, as we are concerned with relative velocities over small distances of typically a few arcseconds. For further details on observations and data reduction see Paper I and references therein.

Throughout this paper all positions are given in arcseconds east and north relative to the star TCC0016, which itself is situated at $05^{\text{h}}35^{\text{m}}14^{\text{s}}.91$, $-05^{\circ}22'39''.31$ (J2000).

3. Data analysis

3.1. Identification and characterization of emitting zones

Data pertaining to the 193 regions analyzed here, are collated in tables A.1 – A.3. All flows are designated by number in these tables. The tables each refer to one of the three regions into which the full region has been subdivided, namely Peak 1, Peak 2 and Region B.

Features were identified on the basis of their brightness and our concomitant ability to locate region boundaries. Thus all regions show a well-defined localized increase in brightness compared to the surrounding gas. Each of these regions has been examined for evidence of a local gas flow. This was done by making 3D-images of each region, where these images show radial velocity and emission brightness as a function of the position in the plane of the sky. Two illustrative examples of regions exhibiting flows are shown in Figs. 3a and b, where the x- and y-axes give the position in the plane of the sky and the z-axis shows the radial velocity of the gas. A colour code associated with every image shows the observed brightness as the number of counts per exposure of 400 s. This can be converted to brightness through the use of the value of $3.0 \pm 0.15 \times 10^{-5} \text{ W m}^{-2} \text{ sr}^{-1}$ found in Vannier et al. (2001) for the brightest region observed here.¹ Using this value it is found that a count of 100 over the 400 s exposure corresponds to $\sim 3.5 \times 10^{-6} \text{ W m}^{-2} \text{ sr}^{-1}$. This conversion may be applied to all regions (and all figures in this work) with the proviso that systematic errors may arise through differing conditions of airmass and of the atmosphere prevailing at the times of observation.

Fig. 3a clearly shows a very localized increase in the radial velocity² and the brightness. The typical extent of the areas which show this phenomenon of strong localised brightness is $0.5''-1''$ in all the 193 regions identified in the data. All regions are therefore well resolved, given a spatial resolution of $0.18''$.

Data for each region have been characterised in terms of the following properties.

¹ The brightest region is in Peak 2 at coordinates $15.82''$ E, $-1.61''$ N, see table A.2, flow no. 2-10.

² In the remainder of this article, velocity should be taken to mean the radial velocity, unless otherwise specified.

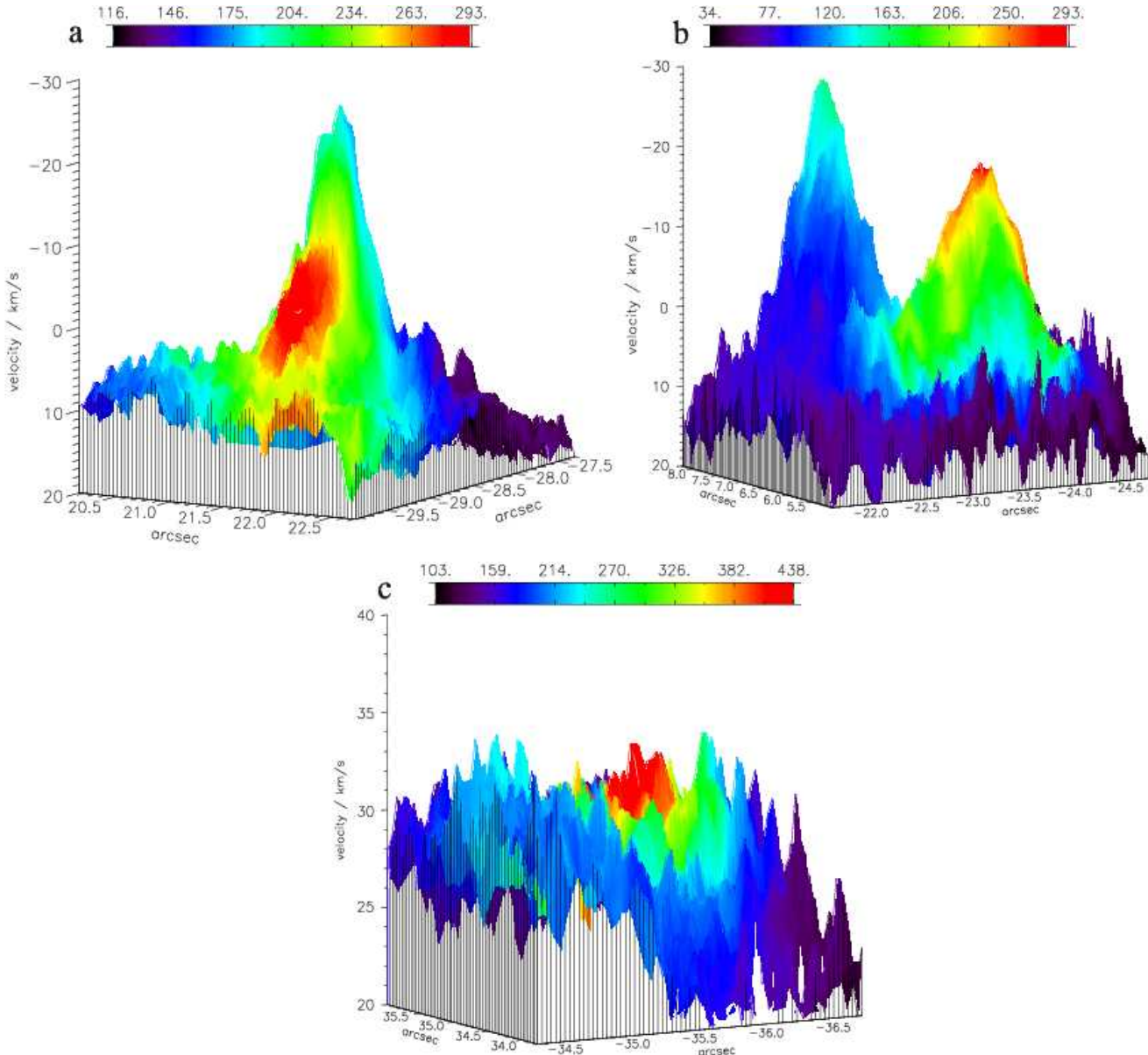


Figure 3. **a** Flow no. 1-61: see table A.1. The vertical axis shows v_{lsr} in km s^{-1} . Colours denote brightness as shown on the colour bar above, in counts per 400 sec. The plane of the sky is shown in arcseconds, relative to TCC0016. **b** Flows no. B-44, B-45 and B-46: see table A.3. Otherwise as in **a**. **c** Flow no. 1-74: see table A.1. This is an example of a flow which shows no clear velocity peak exceeding 5 km s^{-1} .

- (i) the maximum velocity relative to the surrounding gas,
- (ii) the maximum brightness,
- (iii) the displacement in the plane of the sky between the maxima in velocity and brightness.

(i) The maximum velocity of the flow relative to the surrounding gas is found by taking the maximum velocity recorded in the region of interest and subtracting the average velocity of the surrounding gas. The latter may be estimated with a typical uncertainty of $3\text{-}4 \text{ km s}^{-1}$ (see sect. 2). The resulting flow velocity contains this uncertainty. Thus these velocities are less accurately determined than relative velocities between adjacent

bright regions. Using Fig. 3a as an example, the velocity of the surrounding gas is $8\pm3 \text{ km s}^{-1}$. The tip of the velocity peak is at $-24\pm1 \text{ km s}^{-1}$ and thus the flow velocity relatively to the surroundings is $-32\pm4 \text{ km s}^{-1}$ (3σ).

In 64 out of the 193 regions there is an increase in brightness similar to that found, for example, in Figs. 3a and b, but with no corresponding velocity structure. An example is shown in Fig. 3c. These features will be referred to as features with weak radial velocity components (WRVs). Fig. 3c, which is a typical such object, demonstrates that velocity variations are of the order of less than 5 km s^{-1} , with no clear velocity structure.

This is therefore used as a definition of WRVs, which are defined as those objects with a localized maximum in brightness but which show no velocity excursions from the surrounding gas greater than 5 km s^{-1} . WRVs according to their brightness and extent may arise from flows close to the plane of the sky. However, some of these features could also be bright photodissociation regions (see sect. 3.2). In this connection data for the great majority of WRVs are of sufficiently high signal-to-noise that variations in velocity are real and do not simply arise from uncertainties in velocity determination.

(ii) The maximum brightness is the highest recorded brightness within the confines of any region after the 3×3 boxcar smoothing mentioned in sect. 2.

(iii) Spatial displacements of brightness and velocity features are listed in Tables A.1 – A.3. There exists a strong spatial correlation between the local peaks in brightness and velocity: the distance in the plane of the sky between the two peaks is typically less than the extent of either peak. That is, they overly each other in the great majority of cases, with the maximum in velocity lying within the area where the emission caused by the flow is more than twice the background emission. Figs. 3a and b illustrate this general property that features of velocity and brightness are closely associated in the plane of the sky. The use of these displacement data to determine the orientation of gas motion in the plane of the sky is discussed in sect. 5.1.

3.2. The Origin of the H_2 emission

The mechanism by which the H_2 emission is formed is briefly discussed here. This has already been considered in Vannier et al. (2001), Kristensen et al. (2003) and Paper I. Vannier et al. (2001) described in detail, using the shock models of Wilgenbus et al. (2000), how the brightest regions in the Peak 2 could arise from magnetic (C-type) shock compression of dense gas at pre-shock densities around 10^6 cm^{-3} by shocks travelling at 30 km s^{-1} .

Using shock models and limiting their investigations to Peak 2, Vannier et al. (2001) sought to find if quantitative evidence could be established that shocks have collected enough gas and compressed it sufficiently to overcome the Jeans criteria. This work was therefore directed towards discovering if shock-induced star formation is an active mechanism. Later VLT observations have in fact shown the presence of a 140 AU disk in L-band around the position of brightest emission (15.8" E -1.6" N) where Vannier et al. (2001) concentrated their attention. Therefore a protostar would appear already to have formed at this position and the emission observed was most likely due to outflow from a YSO rather than the much earlier stage of shock induced compression envisaged

in Vannier et al. (2001). While other candidates in Peak 2 may be less compelling in terms of emission brightness and the amount of material within a restricted volume, the mechanism of shock-induced star formation could nevertheless be active elsewhere Peak 1 and Peak 2.

The shock-induced mechanism leads of course to star formation at some time 10^{4-5} years in the future, assuming collapse on a free-fall timescale. In this connection, according to the latest shock models (Le Bourlot et al. 2002; Flower et al. 2003; Kristensen et al. 2003, 2006), the brightest emission ($>10^{-5} \text{ W m}^{-2} \text{ sr}^{-1}$, >300 counts per 400 seconds) may readily be generated by magnetic shocks of typically 25 km s^{-1} impinging on dense gas ($>10^6 \text{ cm}^{-3}$), much as in Vannier et al. (2001). Shocks leading to the formation of the fingers occurred recently ($\sim 10^3$ years ago, Doi et al. (2002)) and the associated shock in dense gas in inner regions of OMC1, such as Peaks 1 and 2 may lead to further star formation, again on the 10^{4-5} year timescale.

Both Kristensen et al. (2003) and Paper I addressed the question of the relative importance of shocks and photodissociation regions (PDRs) in yielding the observed H_2 emission brightness. $\theta^1\text{Ori C}$ generates a UV field, at around 100 nm, more than 10^5 times greater than the standard interstellar field. Detailed models for H_2 emission have been devised, for example in Störzer & Hollenbach (1999), for UV fields of this intensity falling upon dense gas, including advection and photoevaporation (Henney & O'Dell 1999). These models show that the maximum contribution to emission brightness in the H_2 $v=1-0$ $\text{S}(1)$ line from PDRs does not exceed a few times $10^{-6} \text{ W m}^{-2} \text{ sr}^{-1}$, given a line-of-sight normal to the PDR. For this geometry, the PDR contribution to the brightness is therefore no more than 10% to 15% of the maximum observed here. The conclusion is that the brightness due to photoexcitation is a generally minor, though non-negligible contributor to the H_2 emission observed here. This issue is discussed in more detail, with reference to specific regions, in Kristensen et al. (2003).

Possible caveats to the above could be provided by young highly obscured O-stars around which the UV field would be even higher than the standard Orion value and the H_2 would be of very high density. However the resulting H_2 emission would also be highly obscured from our view. Low-mass YSOs of class 2 or 3 may also contribute with 100 nm emission, but a comparison with the catalogues of stellar sources in Muensch et al. (2002) and Lada et al. (2004) (see sect. 5.2 and fig. 17) shows that stellar objects of class 0 or I are only found near strong $\text{H}_2\text{v}=1-0$ $\text{S}(1)$ emission in a few cases. Note that with a few exceptions all of the areas examined in this work have a maximum brightness which is 25% or more of the observed maximum brightness, and all regions showing clear evidence of flows show brightness

above the 15% limit mentioned above for **PDR contributions**. Thus PDR mechanisms are unable to reproduce the observed brightness of H_2 emission. This issue is re-examined briefly in the discussion of weak radial velocity components (WRVs) in sect. 5.3 where other geometries are considered in which PDR activity may play a more significant role.

4. Results

To illustrate the nature of the data collated in Tables A.1 – A.3, all features have been plotted in Fig. 4, where each circle marks an individual feature. The radius of the circle is proportional to the maximum brightness, and the colour shows whether features are red-shifted (red circles), blue-shifted (blue circles) or if WRVs were found to be present (yellow circles).

4.1. Flow velocities

Figure 5 shows the number of flows for a given velocity for Peaks 1 and 2 and Region B. Several properties of the flows are apparent:

(i) The fraction of red-shifted flows is similar in Peaks 1 and 2, with 33% in Peak 1 and 45% in Peak 2. There are thus overall fewer red-shifted than blue-shifted flows. The detection of bright H_2 emission is strongly affected by the local dust optical depth. In dense regions associated with star formation the near-IR may be strongly obscured (Rosenthal et al. 2000). Since the densities may exceed 10^7 cm^{-3} , one hundred to a few hundred AU depth of material is sufficient to obscure H_2 emission. Thus material is preferentially observed emerging from the obscuring dust, rather than retreating into it, that is, blue shifted flows are expected to be detected more readily than red shifted, as found.

(ii) Compared to Peak 2, Peak 1 has a large over-representation of WRVs, as evidenced by Fig. 5a and as is clear from Fig. 4. WRVs in Peak 1 **may** have a different origin than other features in Peaks 1 and 2, arising either from a concerted outflow associated with the BN-IRc2 region and/or with a possible PDR contribution. This is discussed in sect. 4.3 and sect. 5.3.

(iii) the total number of flows in Peak 1 and Peak 2 is 40 in each case, excluding WRVs since these may represent in general a different class of object. Since Peak 2 is less than half the size of Peak 1, the density of flows is correspondingly larger in Peak 2.

(iv) In Region B all flows are blue-shifted and the velocities are distributed around an average value of $\sim -18 \text{ km s}^{-1}$ with a spread of 8 km s^{-1} .

(v) For both Peak 1 and Peak 2 the red- and blue-shifted flows appear clumped around $+10 \text{ km s}^{-1}$ and

-10 km s^{-1} . Recall that velocities are relative to the v_{lsr} . Thus this symmetric distribution is the result we would expect if the origin of the flows is internal to OMC1, be it turbulent motion or outflows from protostars. The velocity dispersion of protostars is only a few km s^{-1} in the Orion Nebula (O'Dell 2001; van Altena et al. 1988). Hence if H_2 emission arises to some extent from outflows from protostars, one would expect to observe a distribution of velocities which reflects the range of outflow velocities, since these greatly exceed relative protostellar velocities. Thus data for peaks 1 and 2 in fig. 5 are consistent with the presence of protostellar outflows.

(vi) Flow velocities lie between a few km s^{-1} and an upper limit of $\sim 35\text{--}40 \text{ km s}^{-1}$ for the radial velocity. Again, on the basis that some of the flows may be associated with protostellar outflows, these figures agree with results from Davis et al. (2001) where flow velocities of $5\text{--}40 \text{ km s}^{-1}$ are recorded for a sample of 9 protostellar zones. The upper limit is consistent with results in Le Bourlot et al. (2002) for the critical velocity at which a C-type shock collapses to J-type, in gas of pre-shock density $10^5\text{--}10^6 \text{ cm}^{-3}$.

(vii) Fig. 6 shows Hubble diagrams for each of the 3 regions, Peak 1, Peak 2 and Region B, plotted as the radial velocities versus distance from source I. The dotted line in fig. 6a represents an age of 1000 years corresponding to the age of the finger system as found by Doi et al. (2002). There is no evidence of Hubble-type behaviour in any of the observed regions. Some of the data in fig. 6a may contain close-in representatives of the finger system, the great majority of whose members lie outside our field as noted earlier. It is clear however that the data provide no evidence that the observed shocks are part of the concerted outflow from a common explosive event with which the fingers are associated. One proviso is that Fig. 6 show only radial velocities. Thus the lack of a distance-velocity correlation does not in itself exclude an origin of the observed emission in some common explosive event. Thus we may observe random azimuthal velocities associated with flow in the plan of the sky, observed here as random radial velocities. In fact we show, by appealing to orientation angles of flows in sect. 5.1.2, that there is some directed flow in Peak 1. We should also recollect the present discussion excludes WRVs. In sect. 5.3, we find that there may be a common origin of the WRVs in Peak 1 and the bullets, again representative of a directed flow to the NW.

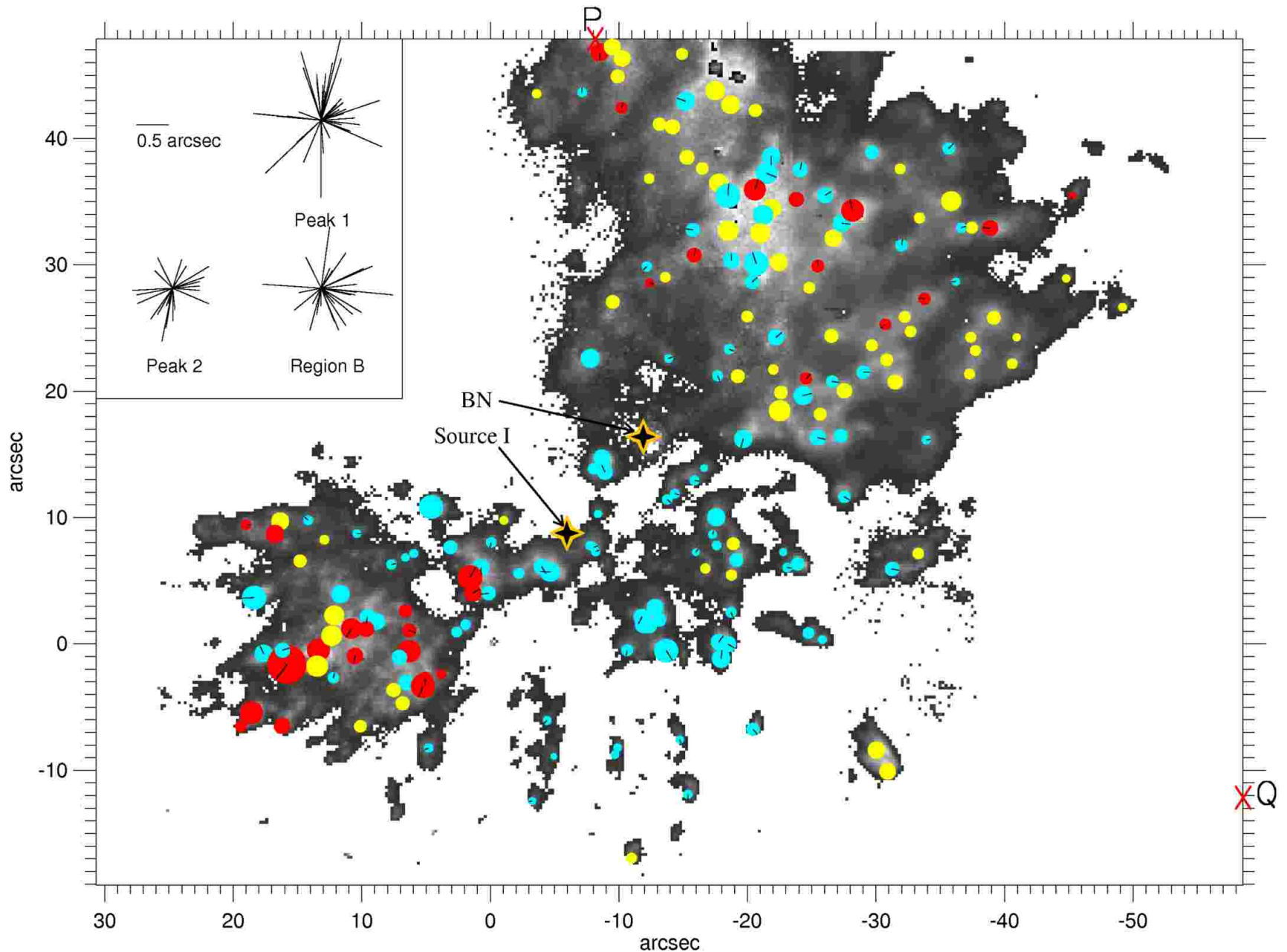


Figure 4. H_2 $v=1-0$ $S(1)$ emission at $2.121 \mu\text{m}$ (gray scale). Circles show all 193 features identified in the present work in this line. The centre of each circle marks the position of maximum brightness of a feature, and the radius of the circle is proportional to the maximum brightness. The colour of a circle shows whether a flow is red-shifted (red circles), blue-shifted (blue circles) or with no clear velocity feature, WRVs – see text, (yellow circles). The position angle of the flow, if determined, see sect. 5.1, is shown by a black line in the circle. The star diagrams in the upper left hand corner show all position angles in a given region. The length of the lines in each star diagram corresponds to the displacement between maximum brightness and maximum velocity. Points P and Q on the main figure axes define the orientations of the line of WRVs across Peak 1 (see sect. 4.3 and sect. 5.3).

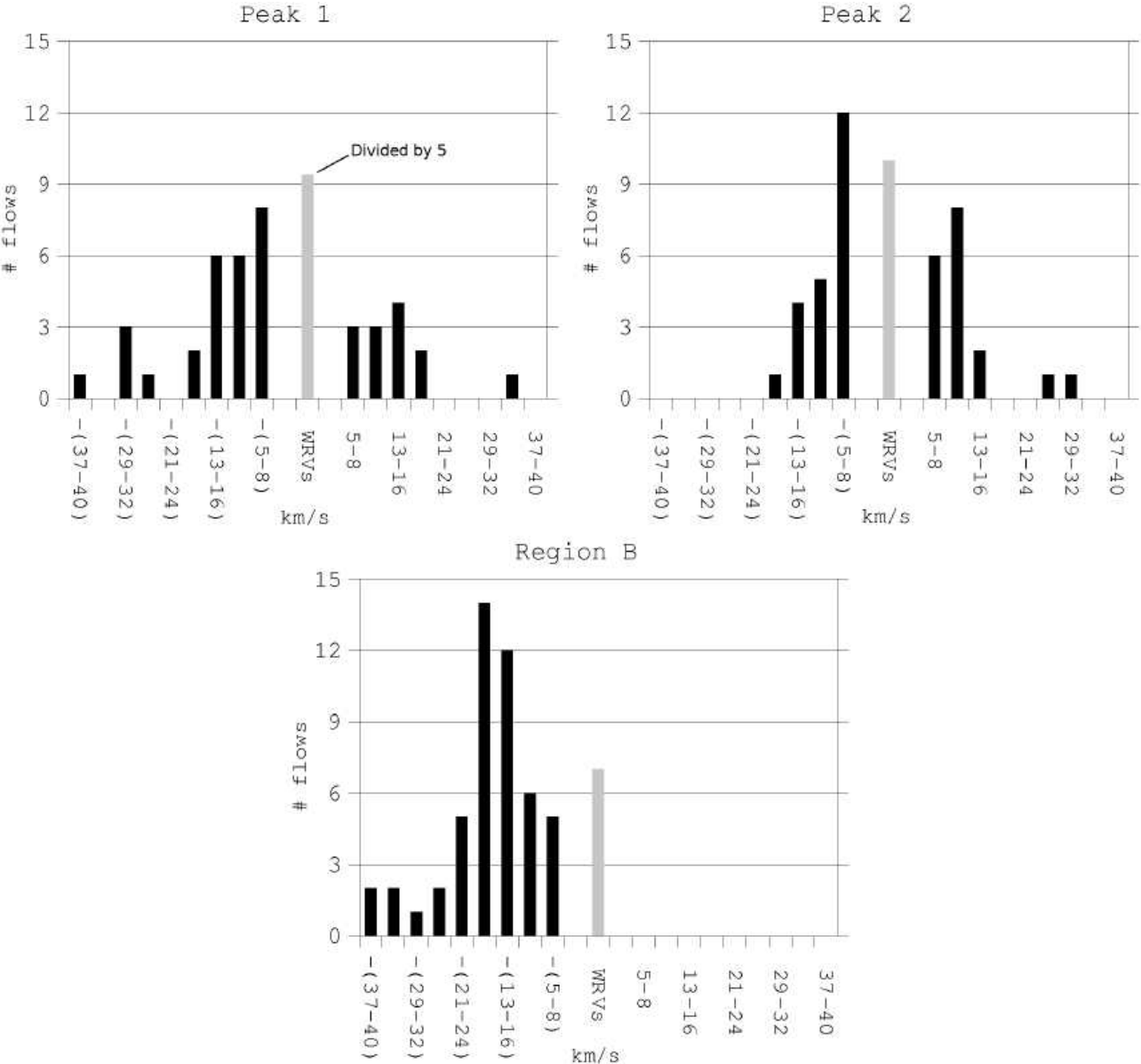


Figure 5. Histograms showing the number of flows with a given radial velocity relative to the velocity of the immediate surroundings in each of the three main regions. Velocities are binned over 4 km s^{-1} , except for WRVs which are inherently binned over 10 km s^{-1} (see sect. 3.1). Weak radial velocity features (WRVs) are shown as gray-shaded bars.

4.2. Displacement of velocity and H_2 emission brightness

Fig. 7 shows the distribution of displacements between associated maxima in brightness and in velocity for each region. We find that for 2/3 of the flows the displacement between maximum velocity and maximum brightness is $\leq 0.6''$, and less than 10% show a displacement of $\geq 1.0''$. This should be compared to the typical extent of a peak in velocity or brightness which is of the order of $0.5''-1''$. Data in Fig. 7 quantify the earlier statement that a strong correlation exists between the positions of maxima in brightness and velocity (sect. 3.1), implying that these

are connected phenomena.

4.3. Spatial distribution of flows with weak radial velocity components (WRVs)

Several features are apparent in the spatial distribution of WRVs.

(i) WRVs comprise only a small proportion of the total number of flows in Peak 2 while in Peak 1 they outnumber all of the flows identified.

(ii) If the assumption is made that the WRVs arise

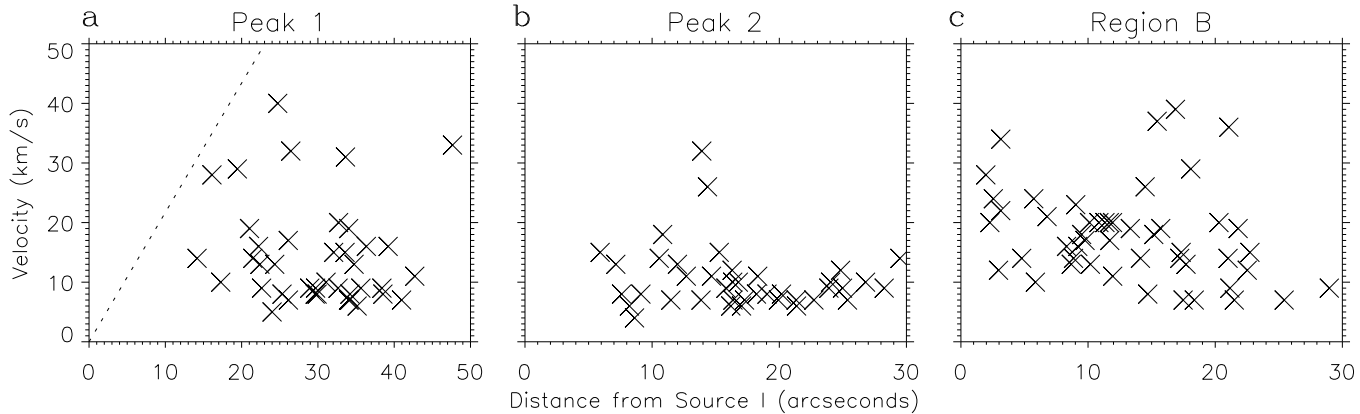


Figure 6. Hubble diagrams showing velocity versus distance from Source I for each of the 3 regions. In a, the dotted line corresponds to an outflow of age 1000 years corresponding to the age of the OMC1 fingers according to Doi et al. (2002). Note that the WRVs are not included in these diagrams since these have no measurable radial velocities.

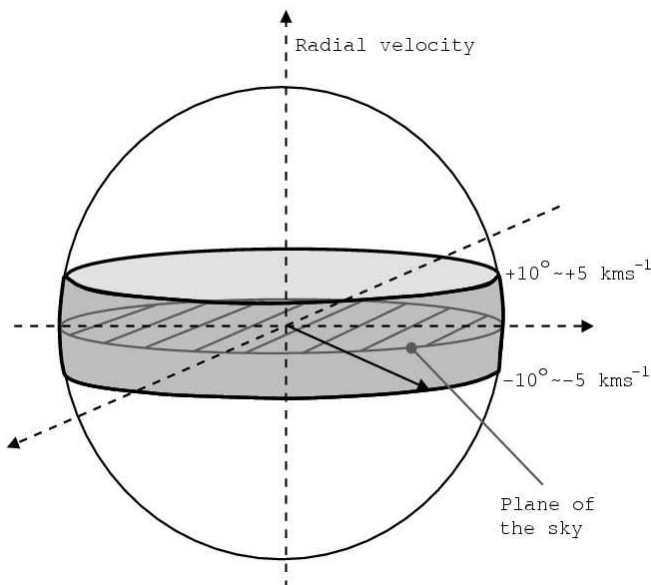


Figure 8. Illustrating the ratio of the number of flows showing less than 5 km s^{-1} radial velocity (WRVs) to the total number of flows: see sect. 4.3 and Eq. 1.

from shock excitation involving clumps of gas moving in or very close to the plane of the sky, then there is an inhomogeneous distribution of motion within Peak 1. This may be shown as follows.

If the general flow pattern in Peak 1 were homogeneous in three dimensions, then an estimate may be made of the number of flows that are expected to fit into the category of WRVs. Given that typical shock speeds in OMC1 are $\sim 30 \text{ km s}^{-1}$ (as suggested by results in Vannier et al. 2001), then the limit imposed on the radial velocity to define a flow as a WRV, $v_{\text{radial}} < 5 \text{ km s}^{-1}$, sect. 3.1, corresponds to flows moving within approximately $\pm 10^\circ$ of the plane of the sky. This is illustrated in Fig. 8. For a

homogeneous distribution of flow direction, the number of flows designated as WRVs relative to the total number of flows should equal the relative area of a band on a sphere around the equator from -10° to $+10^\circ$ ($= \pi/18 \text{ rad.}$):

$$\frac{\text{no. of flows in the plane of the sky}}{\text{total no. of flows}} = \frac{\int_{-\pi/18}^{\pi/18} 2\pi \cos \theta d\theta}{4\pi} \approx 0.17 \quad (1)$$

In Peak 2 a total of 50 flows (including WRVs) are found and thus in a model of homogeneously directed flows, 8–9 WRVs are expected. This agrees well with the 10 examples observed. The same model applied to Peak 1 suggests that ~ 15 WRVs should be seen. However 47 WRVs are observed in Peak 1. The above results do not change significantly if a typical shock speed of 25 or 20 km s^{-1} is assumed instead of 30 km s^{-1} . Thus the flows do not form a spatially homogeneous sample in Peak 1 but lie preferentially in the plane of the sky and appear disproportionately as WRVs.

(iii) The data in Fig. 4 show not only that there is a considerable excess of WRVs in Peak 1 but also that there is the appearance of a concentration of WRVs along a direction on the eastern side of Peak 1 from $-8''$ E, $47''$ N to $-31''$ E, $21''$ N along the line connecting points P and Q in Fig. 4. This line (or slit) is $\sim 30''$ long but only a few arcseconds wide. To assess whether this is a genuine feature of the data or merely a trick of the eye, a slit of length $30''$ and width $2.5''$ has been placed at all positions and for each position at all angles over the data for Peak 1 in Fig. 4. In each case the number of WRVs has been counted within the slit. Figure 9 shows the number of WRVs in the slit at the optimum angle in the sky to pick up the maximum number of WRVs, that is, 140° measured clockwise from N, as a function of the perpendicular distance of the slit from TCC0016. This corresponds to the slit being placed along lines parallel to the line connecting points P and Q in Fig. 4. The

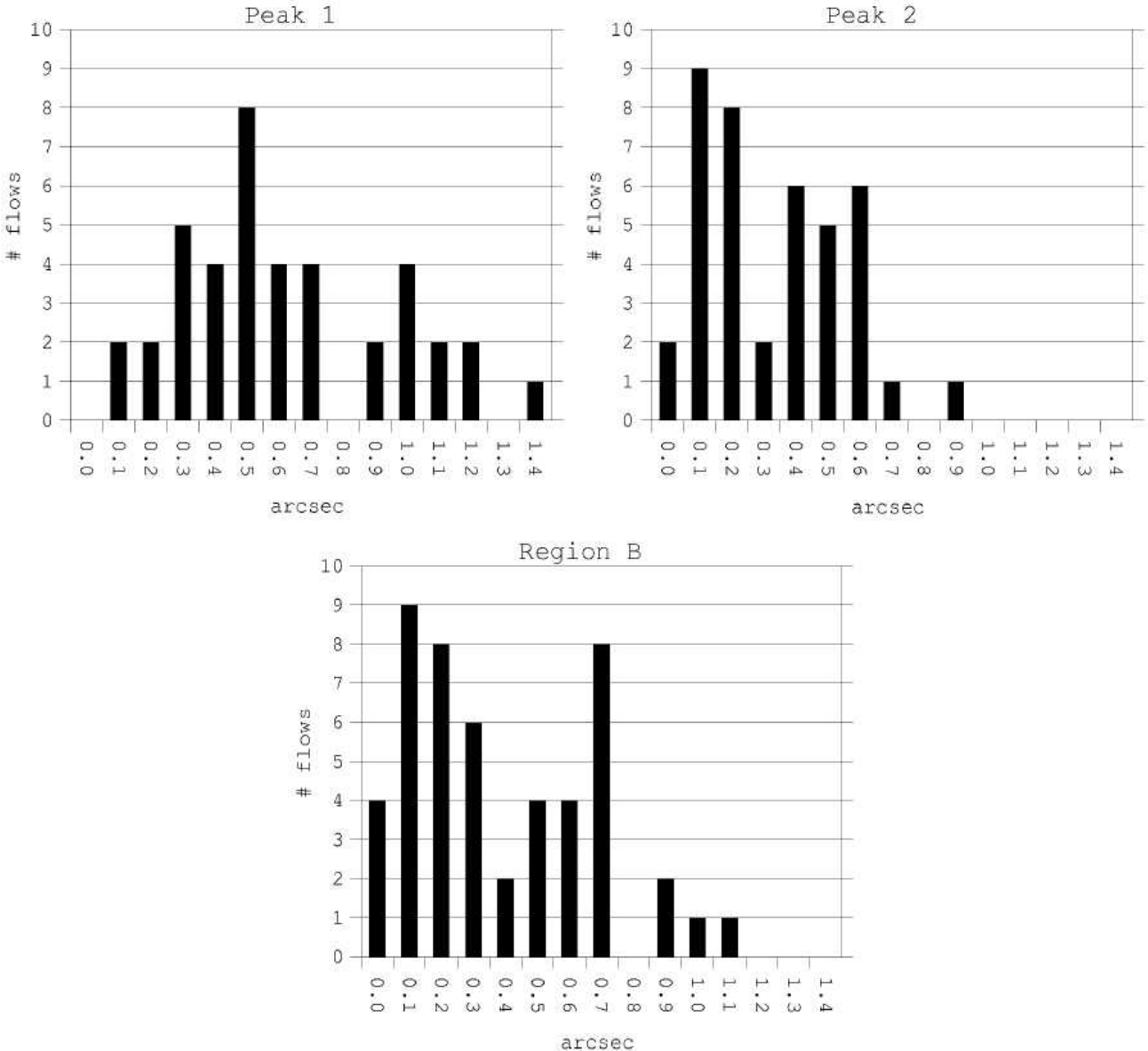


Figure 7. Numbers of flows with a given displacement between the maxima in brightness and velocity for each of the three main regions.

presence of a very clear maximum maximorum indicates that there is a genuine concentration of WRVs at the position designated. There is thus some kind of "front" of emission features at this position.

(iv) A further property distinguishes the WRVs from other features in the field within this concentration or front just identified. An investigation of the morphology of the H₂ emission in these features reveals that $\sim 2/3$ of these objects show a very much more broken up morphology than that typically seen in features elsewhere in Peak 1 and Peak 2, for which emission is clearly associated with radial motion. Moreover, even in other WRVs, outside of this concentration, such a broken up morphology is only seen in 10-15% of the cases. The broken-up morphology

associated with the concentration of WRVs is illustrated in Fig. 10b. This may be compared to the relatively uniform increase towards a single maximum seen in most other WRV objects such as the WRV shown in Fig. 10a. The origin of broken-up structure is briefly considered in sect. 5.3.

4.4. Grouping of flows

In the present section all flows in Fig. 4 are considered save WRVs. Fig. 11 shows how many blue- and red-shifted flows lie within a distance of 1200 AU (2.6'') from any given point, where each flow is represented by a circle of radius 1200 AU. A radius of 1200 AU was chosen because a region of 2000-2500 AU is a typical scale for a star form-

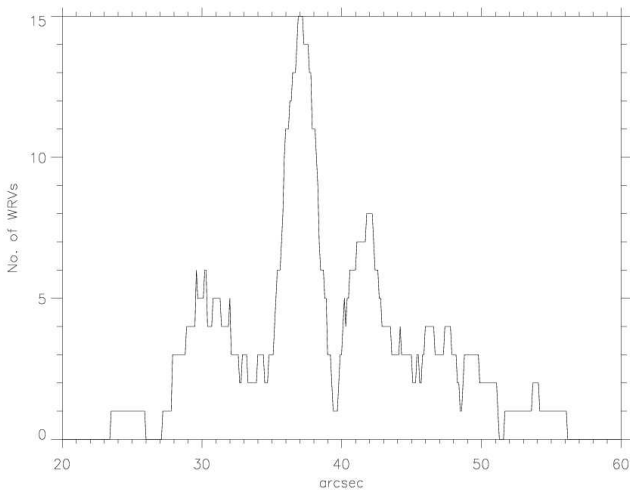


Figure 9. The number of WRVs in a slit placed across Peak 1 at an angle of 140° measured clockwise from N as a function of perpendicular distance between the slit and TCC0016. The position of the peak at $37''$ corresponds to a slit placed along the line connecting points P and Q in Fig. 4.

ing core in the early stages of star formation, e.g. Bate et al. (2003); Delgado-Donate et al. (2004) and this is also the scale where Gustafsson et al. (2006) find deviations in the turbulent velocity structure, showing the presence of a preferred scale. Fig. 11 illustrates whether the flows have a tendency to be grouped together or are spaced equally across the entire area. Peak 1 and Peak 2 show different character. In Peak 1 the flows are distributed rather evenly across the entire area, with only one position showing a large number of flows in a small area, around the position $-22''$ E, $36''$ N. In Peak 2, flows are more grouped with some areas showing 6-8 flows within an area of ~ 2500 AU in diameter around positions $1''$ E, $5''$ N and $9''$ E, $1''$ N. Taken together with the observation, reported in sect. 4.1, that the spatial density of flows is approximately twice as high in Peak 2 as in Peak 1, this points towards Peak 2 being a more active region compared to Peak 1: see also sect. 5.2.

4.5. Further characteristics of the outflow in Region B

As noted, all flows are blue-shifted in Region B and the mean of the velocities is significantly greater than in Peaks 1 and 2. Moreover Region B contains, among the 49 objects in total, five clear examples of bow shocks, based on the morphology of the H_2 emission. An example is displayed in Fig. 12, the left-hand panel of which shows a NAOS-CONICA adaptive optics image obtained with the VLT (Lacombe et al. 2004), lacking velocity data but showing the morphology in graphic detail, and the right hand side showing the GriF results, including velocity data as contours.

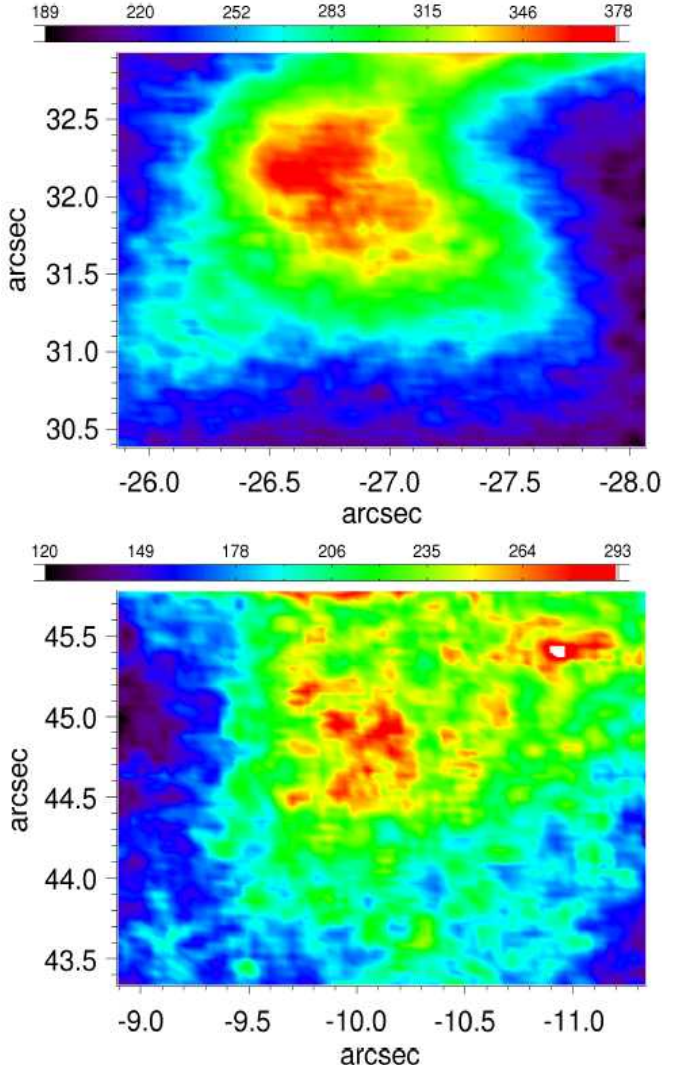


Figure 10. **a** Flow no. 1-57: see Table A.1. A smoothly structured WRV situated in Peak 1 but not in the flow front described in the text: sect. 4.3. **b** Flow no. 1-7: see Table A.1. A highly structured WRV feature lying in the flow front. **Colours denote brightness as shown on the colour bar above, in counts per 400 sec.**

The structure in Region B appears at first to consist of disconnected fragments of emission. However on closer examination it is found that there is widespread weak emission connecting some of the prominent bright features shown in Fig. 4. An example is shown in Fig. 13. A ridge of very weak emission, at the level of 30-60 counts per 400 seconds, corresponding to velocity uncertainties of $3 - 6 \text{ km s}^{-1}$, can be identified connecting three bow-shocks showing blue shifted velocities between -10 and -30 km s^{-1} . Thus the outflow region represents a concerted bulk motion, though diffuse in places.

5. Discussion

Gas flows within OMC1 are of two types. The first is large scale flows. Two such flows may be identified in OMC1.

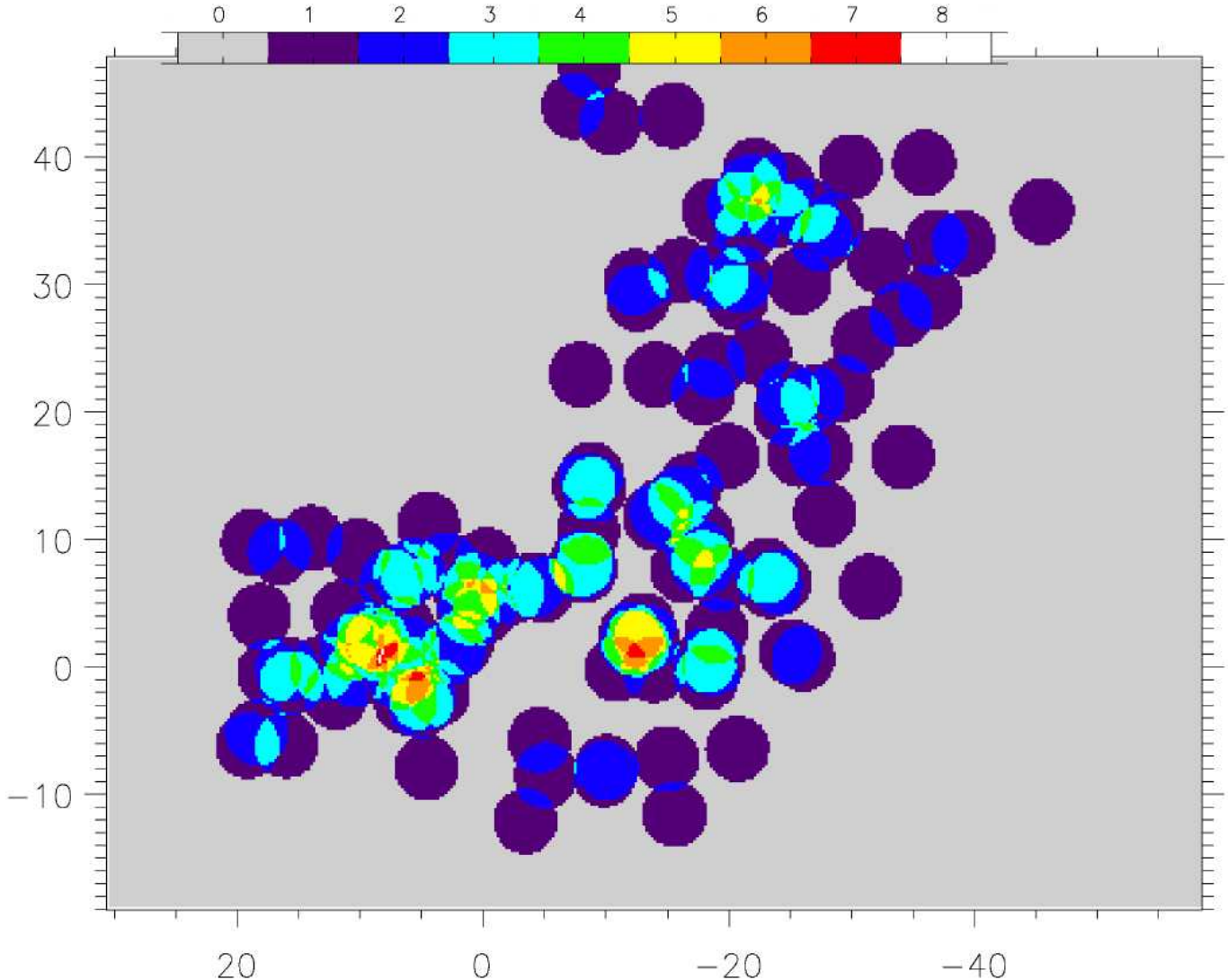


Figure 11. Spatial density of emission features associated with flows, showing the number of flows within ~ 1200 AU of any given point. The colour scale illustrates the number of overlapping features at any point. See sect. 4.4 and sect. 5.2. Axes are labelled in arcseconds.

There was a large-scale outburst ~ 1000 years ago (Doi et al. 2002) roughly in the plane of the sky, which has lead to the subsequent formation of fast moving fingers and bullets in the outer reaches of OMC1 to the NW e.g. Lee & Burton (2000); Doi et al. (2002). The WRVs concentrated in Peak 1 may be part of this scenario, as we discuss in sect. 5.3. The flow identified here in Region B constitutes the other large scale feature. By contrast, this is largely out of the plane of the sky. The relationship between these two outflows is not presently clear. The outflow in Region B is discussed in detail in sect. 6.

The second type of feature is small-scale flows, associated with local low mass star formation. Flows in this case, taken as a body, would be expected to show no overall preferential direction of motion within the plane of the sky, with each site or group of sites acting independently of any other. This point is examined in sect. 5.1 below.

5.1. The physical nature of shocks in OMC1 and their orientation in the plane of the sky

This section considers how data for the displacement of the maxima in velocity and brightness in any chosen feature, recorded in the final column of Tables A.1 – A.3, may be used for the determination of the orientation of shocks in the plane of the sky. To enable this interpretation, it is necessary to consider the brightness and velocity structure of C-type shocks and the spatial relationship between the regions of maximum velocity and maximum brightness in H_2 emission.

5.1.1. A brief overview of shock structure

The following gives a simplified description of the general events at play in a shock. This description is only applicable to features in OMC1 in

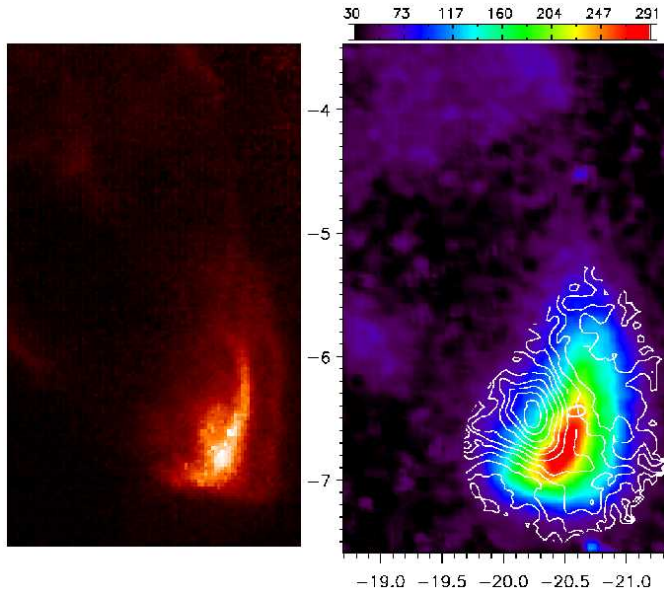


Figure 12. Left hand panel: a VLT image of flow no. B-43, Table A.3, taken with the NAOS-CONICA adaptive optics system, with a spatial resolution of ~ 35 AU: see Lacombe et al. (2004). Right hand panel: the same object obtained with the GriF instrument on CFHT, with a spatial resolution of 70 AU. Contours show velocity and colours show brightness in counts per 400 sec. The maximum in velocity is -36 km s^{-1} at $-20.2''$ E, $-6.5''$ N. The interval between contour lines is 4 km s^{-1} .

broad outline but presents a physical picture which should prove helpful in interpreting our observations. We envisage the shock forming as follows: in a time dependent picture, starting at time zero, before the shock has been created, a jet of gas, from hereon for simplicity considered continuous, is ejected from a protostar and collides at a super-Alfvenic relative velocity with a dense clump of gas in the surrounding medium. The jet slows, energy is given up to the system as heat, and H_2 in the impacted gas is sufficiently excited that emission takes place in IR vibrational bands. C-type shock simulations show that the gas that emits most strongly is moving at a velocity of about ten km s^{-1} less than that of the initial jet. For example, there may be a jet with an initial velocity of 20 km s^{-1} impinging on gas with a pre-shock density of 10^6 cm^{-3} . In the steady state which eventually forms, the heated gas emits most brightly in H_2 when the flow has slowed to $\sim 10 \text{ km s}^{-1}$, according to C-type shock models (Wilgenbus et al. 2000; Le Bourlot et al. 2002; Flower et al. 2003, L. Kristensen, private communication). The gas however continues to emit in vibrationally excited states of H_2 at even lower velocities.

As the initial collisional process described above takes place, more gas is entering the system from the continuous jet. This newly arrived portion of the jet encounters gas which is moving several km s^{-1} more slowly. Where these two portions of the flow meet, there forms a structure called the "Mach disk", which is itself a shock, given that

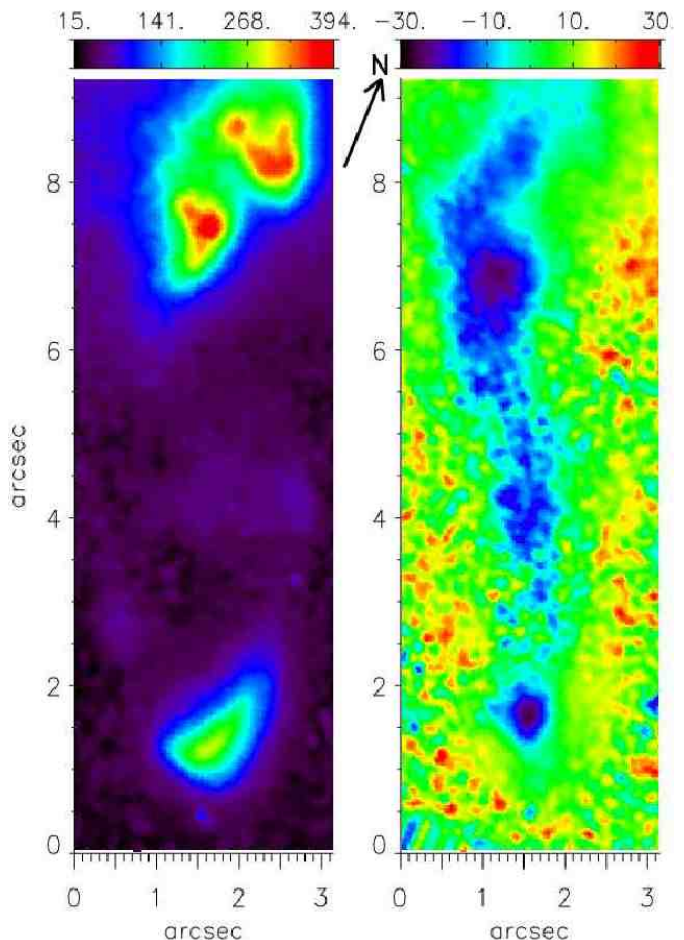


Figure 13. GriF data for three bow shocks within the outflow Region B. Left-hand image: H_2 emission brightness in $v=1-0 \text{ S}(1)$. Colours denote brightness in counts per 400 sec. Right hand image: velocity data for the same field. The colour scale show velocity in km s^{-1} . The orientation of the images is such that north points at an angle of 24° measured clockwise as indicated on the figure. The objects involved, lying $15''$ to $20''$ SW of Source I (see Fig. 4) are B-43 to the south (see also Fig. 12) and B-35–37 in the north, see Table A.3.

the relative flow speeds are super-Alfvenic. Thus there are, to use the model of Raga & Cabrit (1993), effectively two shocks, one at the Mach disk, and one around the apex of the system where the gas is impacting the ambient material. The gas flows in front of and around the outside of the Mach disk, forming a bow structure with so-called "working surfaces" at which weaker shocks form in 3D around the region of the Mach disk. This is illustrated in Fig. 1 of Raga & Cabrit (1993). In all parts of this flow, the gas cools and emits: hence the structure is seen in H_2 emission.

This general model finds support in our observations through the fact that the physical apex of the shock, where it can be identified, is not where the highest velocity is found. The physical tip of the shock has slowed down, following momentum conservation taking account of the

compression of the gas ($\rho_1 v_1 = \rho_2 v_2$). From our observations we find that typically the tip of a bow shock is at a velocity between 1/2 and 1/3 or lower of the maximum velocity. When a magnetic field is present, as here, the working surface becomes a greatly extended zone whose dimensions may be several hundred AU or more, but are typically 50-60 AU in high density regions of (say) 10^6 cm^{-3} (Wilgenbus et al. 2000; Le Bourlot et al. 2002; Lacombe et al. 2004).

Following the above model, the Mach disk is in general the point of highest velocity in the shock relative to the surrounding gas, assuming a constant jet playing on the medium. The question arises, is the Mach disk brighter or less bright in H_2 emission than the portion of the gas in front of it, which is moving more slowly? One might suppose that the brightest emission would tend to lie in front of the Mach disk, since it is in front of the disk that bulk energy is being turned into heat. However in C-type shocks, as in OMC1 (Vannier et al. 2001; Kristensen et al. 2006), the extended shocked zone may well cause the Mach disk to merge with the bow region. A quantitative understanding of the velocity-brightness structure of C-type shocks requires high density models which include both chemistry and at least 2D hydrodynamics. At all events no double maxima in the brightness structure of shocks are seen in the present observations.

In the above we assume a stable continuous system generated through a stable jet of constant speed. The exciting jets cannot be readily identified as distinct structures in OMC1 but where they are observed in class 0 and class I object, protostellar jets may appear time-variable in their velocity (Bontemps et al. 1996; Stanke 2000; Bally et al. 2000; Larson 2003). This would produce a more complex shock structure with several emission maxima, but does not in itself involve any shock formation mechanism fundamentally different from that outlined above. One point to be noted regarding variable jets speeds is that this can result in both forward and backward facing, or reverse, shocks. Reverse shocks are thought to be formed when an initially slow wind becomes a fast wind which then overtakes and compresses the material ahead of it. This gives rise to clumped material where the fast jet impinges on the slower jet. In the limit of a variable jet, the jet consists of spatially separated clumps of material each of which individually forms independent shock structures. This is illustrated in fig. 1 of Hartigan (1989).

A further point is the relative dimension of the jet compared to that of any clump of material on which it impinges. In an idealized view, forward bows are formed when the jet radius is smaller than the dimension of the slow-moving medium and reverse bows form when dimension of the obstacle is smaller than that of the jet.

5.1.2. Determination of orientation angles

On the basis of the previous section the brightest emission and the highest velocity are expected to be closely spatially associated. The shock travels in a direction from maximum velocity to maximum brightness. This model will be referred to as the velocity to brightness model. In some cases observations clearly support this model. An example is shown in Fig. 12, object B-43, Table A.3. Here the maximum velocity is spatially displaced from the maximum brightness by $0.3''$ and the object gives every appearance of a bow shock travelling in the direction of maximum velocity to maximum brightness. A counter-example to the above is however furnished by object 2-20 in Table A.2. Here the bow shape of the emission suggests motion in a NW direction, whereas application of the velocity to brightness model for the shock motion indicates motion in the SE direction. Furthermore, in areas with a high spatial density of flows, perhaps indicative of a multiple star forming region (see sect. 5.2), closely situated pairs of outflows where one is red-shifted and the other blue-shifted are seen. However, for all pairs of red- and blue-shifted shocks where position angles are determined by the maximum velocity to maximum brightness flow direction model (see below), the flows appear to be converging in the plane of the sky. If any pair of flows formed a bipolar outflow, they would clearly be expected to be found diverging, that is, moving apart from one another. An example of this discrepant behaviour may be found in Fig. 18a showing flows 1-76 and 1-81 (see Table A.1).

Failure of the velocity to brightness model will arise if effects of optical depth are paramount in determining the location of maximum brightness. The brightness of emission is a function not only of the local efficiency of excitation associated with local loss of kinetic energy, but also of the column density of gas which is observed. Thus a shock travelling at some arbitrary angle may appear brighter behind the position of maximum velocity by virtue of its bow form, although locally the emission is weaker than at the tip of the shock, where the latter is of low column density. This model is illustrated in Fig. 14, and was described in Paper I. This model will be referred to as the column density model.

The common feature of both models is that the maximum in emission and the maximum in velocity lie on a vector defining the orientation of the shock in the plane of the sky. However, in the absence of a full 2D or 3D C-type shock code for H_2 excitation including chemistry, it is not possible to determine which processes and thus which model may be relevant in any particular case, save where the morphology clearly indicates a bow shock (as in Fig. 12). Tables A.1 – A.3 quote position angles measured east of north (i.e. counter-clockwise) based on the velocity to brightness model where shocks are travelling in the direction from the position of maximum velocity to the position of maximum brightness in the plane of the sky. However, with a few exceptions where the morphology of the flow would appear to dictate the absolute position an-

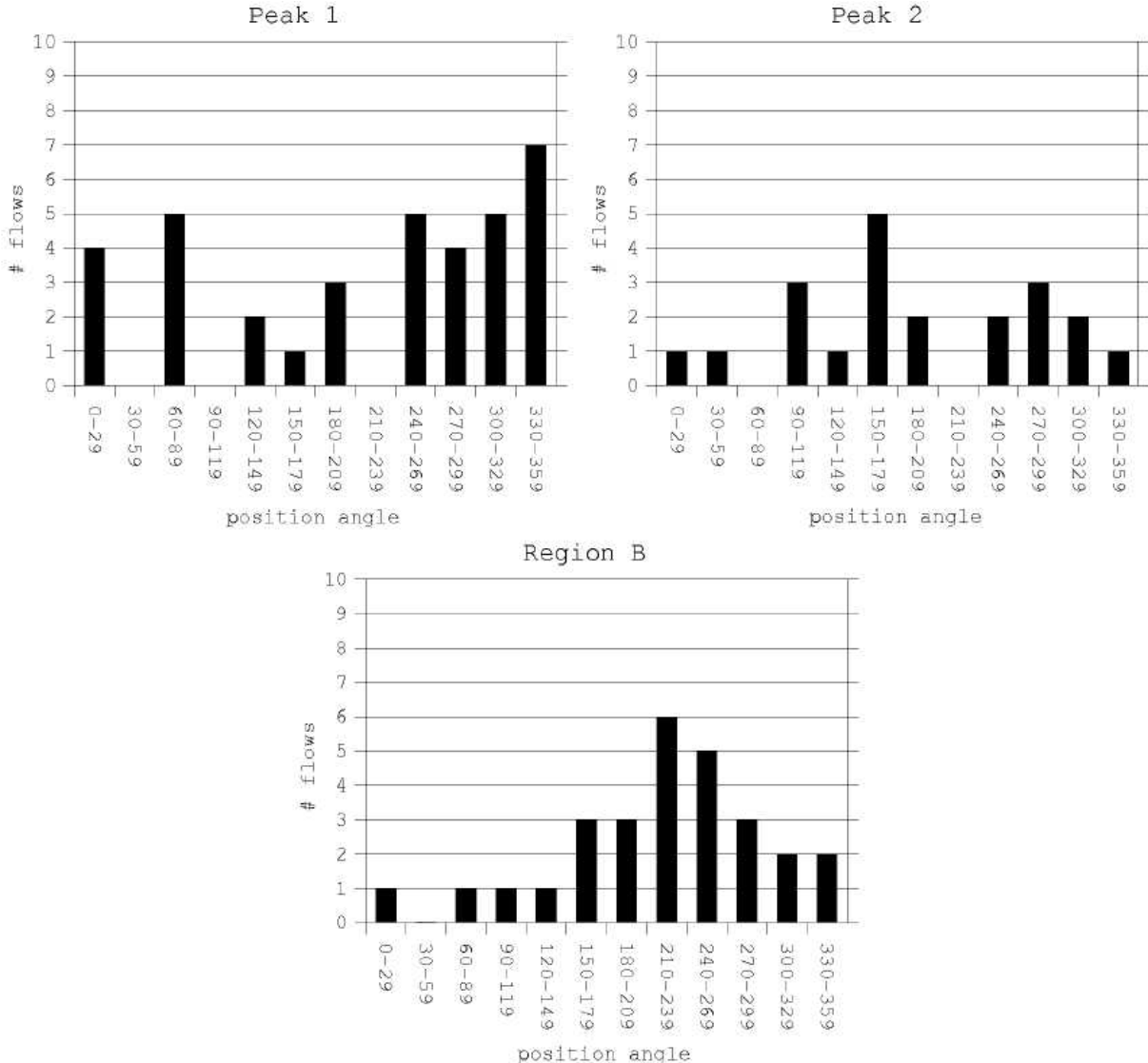


Figure 15. Number of flows in each of the three main regions with position angles in a given range (see also star diagrams in Fig. 4).

gle, e.g. fig. 12, these position angles are uncertain by 180° with respect to absolute direction as discussed above. The exceptions are marked with a star and are found only in Table A.3 for the outflow region B. The uncertainty in the position angle is estimated to be $\sim \pm 25^\circ$, decreasing with increasing displacement. The uncertainty stems from the determination of the exact positions of the maxima. A displacement of $<0.25''$ of maximum brightness and maximum velocity is close to the resolution limit, and small variations in displacement would have a large influence on derived position angles. Position angles are therefore only determined where the displacement is $\geq 0.25''$.

An important consideration is whether the position angles are dominated by a general outflow motion from the BN-IRc2 area or are approximately isotropic in distribution in each main region (Peak 1, Peak 2 and Region B). Fig. 15 show the distribution of position angles binned

over 30° intervals, with the reservation that individual position angles may be incorrect by 180° (see above discussion). In this connection, the assumption has been made that one or the other model for position angles (velocity to brightness model or column density model) will dominate in a given zone, given that a single mechanism causing shocks predominates in any one zone, that is, outflows from star forming regions or a large scale flow impinging on the region (as in Region B). With this assumption, any preferred directions can be found by looking for anisotropies in the distribution of position angles. Rebinning the histograms in Fig. 15 to just two bins of width 180° and then shifting the absolute positions of the bins to cover all possible combinations will show anisotropies as large differences in the number of flows in each bin. This corresponds to placing a line across the star diagrams in the inset in Fig. 4 and counting the number

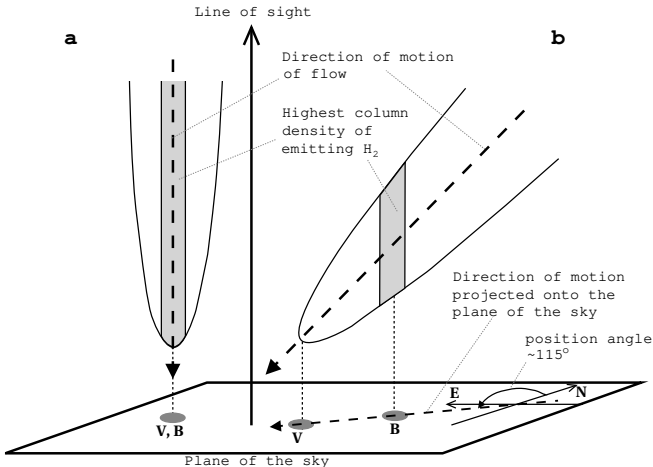


Figure 14. An illustration of the proposed geometry by which position angles are estimated in the column density model (see sect. 5.1.2). V's marks the position of the observed maximum in velocity and B's in brightness in the plane of the sky. **a** a flow moving in the line of sight: the maxima in brightness and velocity coincide. **b** A flow moving at an angle to the line of sight: the maximum in brightness will appear at some point behind the tip of the shock. A vector through the two maxima then gives the direction of the flow projected onto the plane of the sky, the position angle.

of flows on each side of the line. The greatest difference between the numbers above and below the line will appear when the line is perpendicular to the direction of an overall motion, while there will be roughly equal numbers when the line is parallel to any overall motion. If the line is rotated (corresponding to the bins in Fig. 15 being shifted) any preferred direction will appear as a maximum in the ratio between the number of flows on each side of the line at an angle perpendicular to the outflow direction. If there is no preferred direction of motion the ratio should be approximately unity independent of the angle of rotation. Fig. 16 shows this ratio as a function of angle measured counter-clockwise from north for each main region. The ratio is calculated so that it is always ≥ 1 .

Region B (Fig. 16c) shows a high degree of anisotropy around 140–160° and a minimum around 50–70°. As described above, this property with a maximum and a minimum perpendicular to the maximum, indicates that the motions are dominated by an overall outflow motion. In this case the motion is along a line oriented ~ 50 –70° counter-clockwise from north, that is, approximately NE-SW. The nature of this outflow in Region B will be discussed further in sect. 6.

Fig. 16a shows a minimum around 130–160° and a maximum at 20–50°. This is similar to the structure observed for Region B although the maximum is less pronounced. This suggests that the observed flows in Peak 1 are also partly described by an outflow motion (towards the NW in this case), but not to the same degree as in Region B. Finally Peak 2 (Fig. 16b) shows only very weak

Table 1. Good protostellar candidates, "candidates", (upper half of table) and weaker candidates, "possible candidates", (lower half) in the area of OMC1 covered in the present work, based on data taken from Muench et al. (2002). For purposes of cross-reference, we have adopted the numbering of Muench et al. (2002).

Protostellar candidates in OMC1				
Candidates				
Muench et al. numeration	Coordinates		Colour indices	
	rel. to TCC0016		K–L	J–H
00506	-18.3	-17.1	5.77	—
00543	9.5	-7.2	3.29	—
00557	-0.9	-5.0	2.32	$>1.82^a$
00560	-38.4	-2.3	3.03	$>0.82^a$
00569	-24.0	-0.1	3.57	—
00572A	-3.6	0.6	1.52	$>2.67^a$
00576	19.2	1.6	1.77	1.07
00578	-14.6	1.6	4.42	—
00580	4.4	2.4	2.76	3.77
00583	-8.3	3.0	1.50	1.86
00596	14.6	5.9	1.53	1.11
00598	-8.4	6.3	2.99	3.30
00603	-0.6	7.5	2.22	1.02
00614A	-2.9	9.4	2.81	$>4.65^a$
00645	-17.6	17.1	1.82	1.32
00709A	-9.2	34.7	1.99	1.25
00726	-16.7	39.4	2.55	2.94

Possible candidates			
No L band ; H–K > 2.0 or K band photometry only.			
Muench et al. numeration	Coordinates		
	rel. to TCC0016	H–K	M_K
00552	-20.9	-6.1	2.81
00554	-4.7	-5.8	$>2.79^b$
00561	15.8	-2.1	3.43
00570	-5.7	0.0	$>3.00^b$
00585	-10.7	3.4	3.19
00591	-11.1	4.9	3.49
00594	1.5	5.2	$>3.85^b$
00609	-40.8	8.3	$>1.63^b$
00610	-9.2	8.5	6.09
00634	-8.6	14.2	3.35
00665	-17.1	21.7	2.04
00691	-25.1	29.3	3.05
00695	-37.4	30.4	3.13
00698	-44.0	31.1	$>2.91^b$
00713	-47.7	36.1	$>2.99^b$

^a Muench et al. quote a detection limit of 18.15 in J band.

^b Muench et al. quote a detection limit of 17.8 in H band.

maximum-minimum structure, with a distribution of position angles which is close to isotropic. This suggests that the flows observed in Peak 2 are only weakly affected by general outflow motion and tend rather to be individual flows, such as might arise from local star formation.

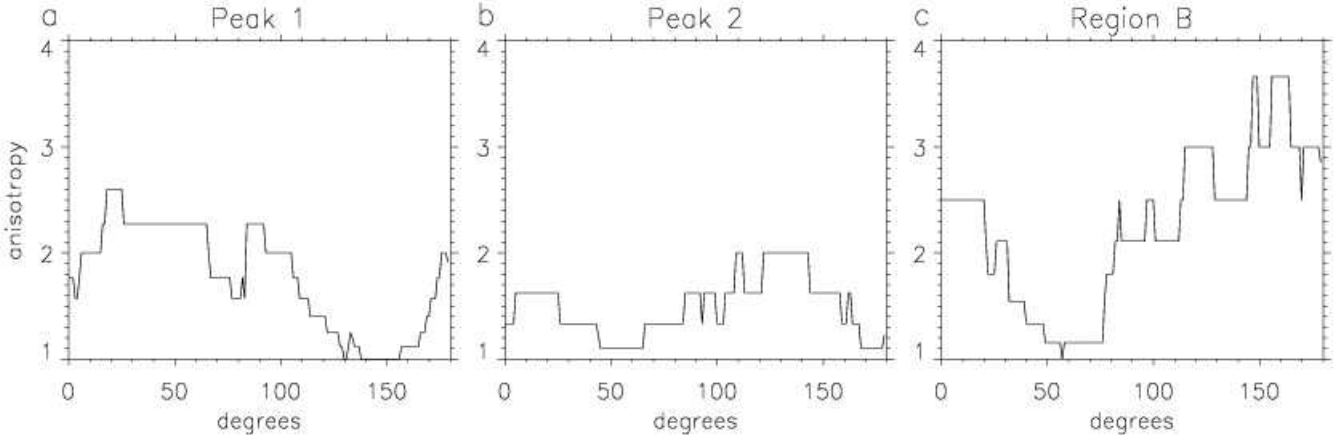


Figure 16. The ratio between the number of flows on each side of a line through the star diagrams in Fig. 4 as a function of the angle between the line and north measured anti-clockwise from north. A high value suggests an anisotropy in the distribution of position angles across the line while a value of unity indicates an isotropic distribution.

5.2. Protostars and Star forming regions in OMC1

Patterns of gas motion and spatial distribution of flows are examined here for Peaks 1 and 2. Our discussion provides further evidence for on-going low mass star formation in OMC1. The major source of energy injection into OMC1 is at 0.1 pc (20000 AU) scales through outflows from massive stars and as part of a large scale cascade of turbulent energy (Gustafsson et al. 2006). Thus many of the flows, both large and small scale, identified in the present work are an expression of the turbulence inherent in the gas through massive stellar outflows from the BN-IRc2 complex (Shuping et al. 2004; Greenhill et al. 2004b) and from source I (see below; Greenhill et al. 2004a). However the gas dynamics may also be influenced by the events which we focus upon here, namely low mass star formation. This would provide an additional source of energy injection and generates flows at smaller scales of a few arcseconds, 1000-2000 AU, through bipolar outflows from isolated protostars or multipolar outflows from multiple star formation (see Figs. 18a-c).

We first consider the IR observational evidence for the presence of early protostars in OMC1. To this end we have compiled a table of protostellar candidates in OMC1 (table 1). We use the criterion reported in Kenyon & Hartmann (1995), for YSOs in Taurus, that an object with $K-L > 1.5$ is almost always of a protostellar nature (specifically class I) and assume that this also holds for Orion. We apply this criterion to the photometry data of Muench et al. (2002) and Lada et al. (2004) for Orion. We furthermore use the criterion that $J-H$ must be > 1.0 to exclude, for example, unresolved binaries (Lada et al. 2000). The resulting protostellar candidates are shown in table 1. For ease of reference we have adopted the numbering system of Muench et al. (2002). Where a " $>$ " symbol is encountered, this implies that J band data are ab-

sent, in the upper section of the table, or H-band are absent in the lower.

We have divided objects into those which are very likely protostars, labelled "candidates" (upper part of table 1) and those where the identification is more tentative, labelled "possible candidates" (lower half of table 1). In addition there are objects for which the colours suggest that they may be excluded as protostars. These are not shown in table 1. This last category forms the majority of point-like objects within our complete field. However within Peaks 1 and 2, these objects occur in roughly equal numbers to the sum of "candidates" and "possible candidates". Fig. 17 shows the positions of all objects in the 3 categories. Candidates and possible candidates have been marked with circles and triangles respectively with their accompanying number for reference to table 1. Non-candidates have been marked with a square. From a comparison with fig. 1 in Shuping et al. (2004) we find that among the objects in table 1 are source n (00598), IRc4 (00585), IRc7 (00610), IRc11 (00614) IRc12 (00603) and IRc15 (00634). Furthermore IRc9 is found to be identical with 00726. Source n is discussed in more detail in section 6. IRc9 will be mentioned in the following section, sect. 5.3.

The term "candidates" covers objects which have $K-L > 1.5$ and which have either $J-H > 1.0$ or where $J-H$ is undetermined. The term "possible candidates" covers objects with $H-K > 2.0$. As far as the authors are aware, the latter is a new criterion for the identification of protostars, motivated by a lack of L-band photometry. The new criterion has been established as follows. An extensive analysis of the H-K colour index of the stars in Muench et al. (2002) has been carried out. It has

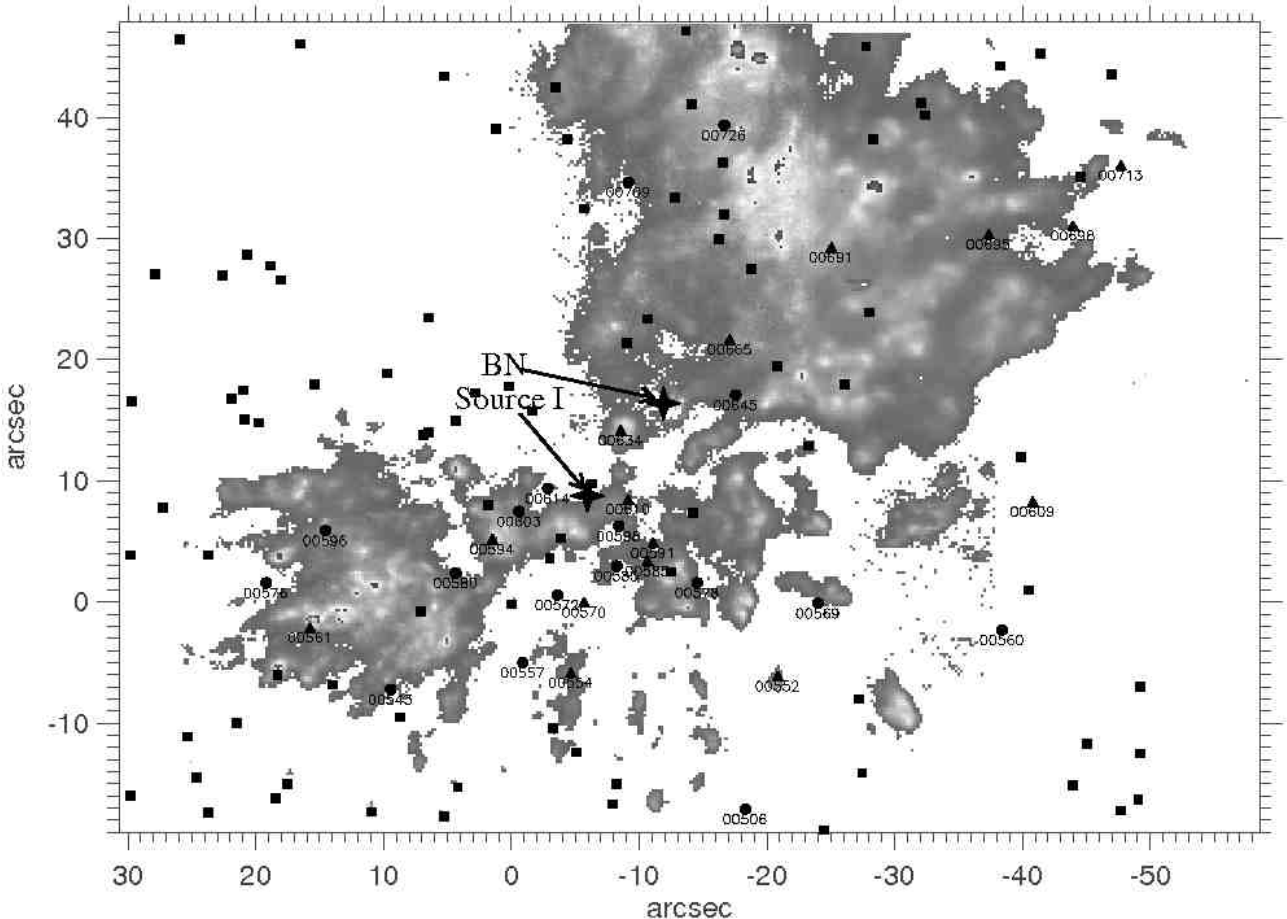


Figure 17. The positions of point-like sources from Muench et al. (2002) in the observed field of OMC1. Objects have been divided into 3 categories based whether they are candidates (circles), possible candidates (triangles) or non-candidates (squares). Numbers refer to the labels in table 1.

been found that for objects with $K-L > 1.5$, 39% have $H-K > 1.5$ and 14% have $H-K > 2$. By contrast, for objects with $K-L < 1.5$ – which are not protostellar candidates – less than 2% have $H-K > 1.5$ and only one object (0.3%) has $H-K > 2$. On this basis a $H-K$ colour index of > 2 is adopted as a tentative identification of "possible protostars" in table 1 and in Fig. 17. We note that the value of $H-K$ cannot however be used to exclude protostellar candidates. In this sense the objects listed in table 1 form a minimum set. Under "possible candidates" in table 1 we also list object from Muench et al. (2002) which have only been detected in K band. These are shown with $H-K >$ some value. The K -band detection, without J and H , suggests that these objects are deeply buried in the dusty gas. We conclude that there 17 good protostellar candidates in our field with a further 15 (or more) possible candidates. A comparison has also been made with the Chandra Orion Ultradeep Project (COUP) X-ray data (Getman et al. 2005; Grossi et al. 2005) and sources in table 1. COUP contains

numerous point sources in the direction of the region studied here and a detailed comparison will be made elsewhere. Suffice it say at present that there is a remarkable correspondence between candidates in table 1 with COUP sources with 14 out of 17 spatial overlaps, whilst the so-called possible candidates are anti-correlated, with only 3 out of 15 spatial overlaps. Overall about half of Muench et al. (2002) sources are spatially coincident with COUP sources.

We now turn to the positional correlation of these objects with possible outflows and H₂ emission in general. In some regions two closely spaced shocks moving in opposite directions are seen, which could indicate that a protostar is situated in between, causing the shocks. An example of this is shown in Fig. 18a, where a pair of flows are found, one red-shifted and the other blue-shifted. Data in table A.1 show that position angles of these flows are roughly 180° apart, noting the indeterminacy with regard to their relative direction. **However**, if the positions of protostellar candidates in table 1 are compared with the positions of candidate bipo-

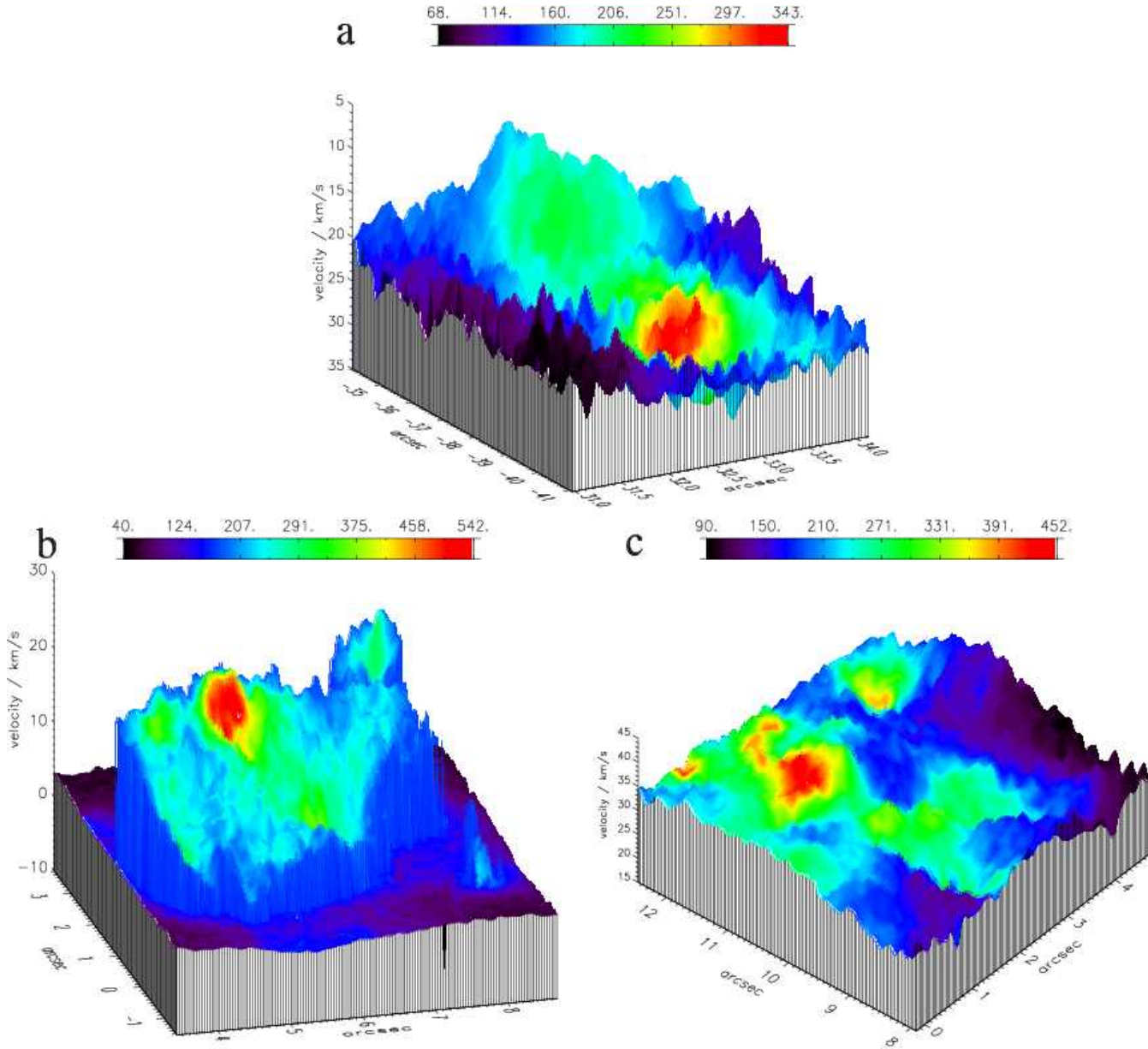


Figure 18. Various areas with multiple flows in a small area: **a** A possible bipolar outflow. Flows no. 1-76 and 1-81: see Table A.1. **b** A complex flow pattern. Flows no. 2-42, 45, 46, 47, 48, 49: see Table A.2. **c** Another example of a complex flow pattern. Flows no. 2-16, 18, 19, 20, 24, 25: see Table A.2. Colours denote the brightness in counts per 400 s exposure.

lar outflows, there is no clear correlation between the two. In only 2 positions, 15.75" E -2.1" N (object 00561, see table 1) and 1.50" E 5.2" N (00594) a candidate protostar appears directly over a pair of flows, whereas in many cases a "bipolar pair" is found where there is no evidence of a protostar. Thus a "bipolar pair" in itself does not appear to be evidence of the presence of a protostar. However the caution should be made that we are considering the earliest stages of protostellar development (class 0/I). This phase is characterized by a very high degree of obscuration, and new, deeper observations than those of Muench et al.

(2002), used here to detect the protostars, may yield different results.

As described in sect. 4.4, there is a marked difference in how flows are distributed in Peak 1 and Peak 2. In Peak 1 the flows are mostly uniformly distributed across the area, whilst in Peak 2 the shocks often appear in small groups of 6-8 shocks within an area of $\sim 5''$ in diameter (see Fig. 11 and Figs. 18b and c), which corresponds to ~ 2400 AU, at the distance of Orion. Since most stars are expected to form as part of a binary or multiple system (Pudritz 2002; Larson 2003), it seems plausible that these groups of shocks indicate places where multiple star formation is ongoing: the presence of 2-3 protostars would account

for 4-6 shocks from bipolar outflows. The flows in these regions are not however generally found as pairs of shocks moving in opposite directions, as may be seen in Figs. 18b and c with reference to the position angles in Table A.2. This supports a picture in which multiple star formation is a complex process involving interactions between the protostars and disks causing jets which are episodic or pulsed (Larson 2003, and references therein).

We now examine whether we can associate regions with large densities of flows, as just mentioned, with protostars listed in table 1. Moving from east to west (left to right) in fig. 11 the first region of high flow density is around coordinates 7° E 0° N. Only one stellar-like object is observed along the line-of-sight to this region: the proplyd 154-240 (O'Dell et al. 1997; Schultz et al. 1999). Since this object has been observed in the visible by HST it cannot be a protostar buried in the dense, dusty gas.

Moving away from a line-of-sight positional correlation of possible protostars and H_2 emission, there is a good protostellar candidate $\sim 4''$ NW or 1600-2000 AU in the plane of the sky. This is the object 00580 (1) which has $K-L, J-H > 2$ fulfilling our criteria for a buried protostar. This is therefore a good candidate to power at least some of the emission that is observed in this highly active zone.

The second region of high flow activity in fig. 11 is around coordinates 0° E 6° N. Within a radius of a few arcseconds there is one star which satisfies the protostellar criteria, namely 00603 with $K-L = 2.22$ and $J-H = 1.02$. There are two other stars for which we do not have L band data available and therefore we are unsure of their nature. One of these is 00594 which is listed in table 1 under "possible candidates". This object lies just outside the Lada et al. (2004) frame. Muench et al. (2002) do not detect this object in J and H and record $m_K = 13.95$. Thus it is a highly obscured object and therefore accordingly appears in table 1. A further object is 00606. This object has no L-band data, and with $H-K = 0.57$ this is not an obvious protostellar candidate. However, one should recall from the above discussion that the $H-K$ colour index is useful only for including, not excluding, protostellar candidates.

We turn now to the third flow concentration, which is centred on $-22''$ E $37''$ N. Surveying the region within a radius of $\sim 4''$, we find the star IRc9 (00726) (Smith & Bally 2005), with $J-H$ and $K-L$ both > 2 , fulfilling the protostellar criteria, see table 1. There is also another object (00715) within a few arcseconds from this concentration of flows, but again there is insufficient photometry to make an assignment as to the nature of this object.

Looking at Peak 1 in general, rather than at concentrations of flows, there are a further two

protostellar candidates, 00645 and 00709A, both situated along the edge of the H_2 emission seen in Peak 1. There are also another 5 possible protostellar candidates (00665, 00691, 00695, 00698, 00713) which are spread across Peak 1. In Peak 2, there are a further 3 protostellar candidates (00543, 00576, 00596), and one possible candidate, 00561, associated with the very bright H_2 emission at $16''$ E $-2''$ N. The object 00561 has in fact an associated 140 AU diameter object observed in the L-band with the VLT (Paper I), as mentioned in sect. 3.2. We note that with the exception of 00561 (in Peak 2) no stars or protostars in Peak 1 or 2 are directly associated with the brightest areas of H_2 emission.

In region B there are 8 protostellar candidates and a further 8 possible candidates. Half of these are situated in the dense core of OMC1 around Source I and may contribute to H_2 emission in this region. The other half are widely distributed over region B.

The discussion here and in preceding sections points towards Peak 2 being a more active star forming region than Peak 1 with similar numbers of protostellar candidates despite Peak 2 being only half the size of Peak 1 in the plane of the sky. This is an unexpected result given the proximity of the two regions. One possible explanation is that the ionization front from $\theta^1\text{Ori C}$ has cleared away most of the diffuse gas in Peak 2, leaving only the densest parts of a previously more extensive cloud and allowing us to see the dense star forming cores which would otherwise have been obscured from view. This interpretation is supported by the work of Pogge et al. (1992) and Takami et al. (2002) who show evidence of an ionization front just north of Peak 2.

The above considerations ignored the presence of WRVs in Peaks 1 and 2. In Peak 2 WRVs form only 20% of the observed flows but in Peak 1, they form more than 50% of the flows. However analysis presented in sect. 4.3, showing the organised nature of WRV flows in Peak 1, suggests that WRVs form a subset of flows which should not be associated with local star formation. This is further discussed in the section directly below, sect. 5.3.

At the start of this section we asked whether H_2 emission might in part be caused by the presence of protostars with associated outflows. Our data show that this is the case but we do not demonstrate that the majority of bright emission is due to protostellar activity in OMC1. By their nature the most important sources may be deeply buried. However for the present we conclude that the emission arises from a mix of protostellar and massive star activity. In particular in Peak 1, present data suggest that emission may be dominated by massive outflow from the vicinity of Source I and the BN region.

5.3. The origin of weak radial velocity structure in Peak 1

The spatial distribution of weak radial velocity components (WRVs) in Peak 1 revealed a band, $\sim 2\text{--}3''$ in width and more than $30''$ long passing diagonally across emission in Peak 1 (see sect. 4.3). It was also noted that 2/3 of these WRVs showed a much more broken-up structure than other features, including other WRVs. This section briefly explores possible scenarios for the origin of this band of WRVs.

The first scenario is that the band of WRVs may represent a less energetic part of the outburst which created the "bullets" or "fingers" (Allen & Burton 1993). These are clumps of gas moving radially outwards at high velocities of up to several hundred km s^{-1} (Doi et al. 2002) and appear to have an origin in the area around BN-IRc2 and Source I (Salas et al. 1999; O'Dell 2001; Doi et al. 2002). If the WRVs are moving at a velocity of 40 km s^{-1} – the upper limit of motions observed here for other clumps of H_2 – in 1000 years they would be found at a position about $18''$ from the BN-IRc2 complex, essentially where they are observed. The typical mass of each WRV can be estimated to be $\sim 1.5 \times 10^{-3} M_\odot$, given a density of 10^7 cm^{-3} and a diameter of 500 AU. This yields a total bulk energy for outflowing hot H_2 in the WRVs of the order of $\sim 5 \times 10^{44}$ ergs, for 20 such objects. This is about 1% of the energy associated with the bullets whose properties are reported in Burton (1997).

A second scenario is that the band of WRVs is the result of bright photodissociation zones powered by $\theta^1\text{Ori C}$, but with enhanced brightness due to geometrical effects (see below). The morphology of the ionization front, described in Wen & O'Dell (1995) and refined in O'Dell (2001), shows that the bright H_2 clumps observed in the present work arise from dense gas within the HII region created by $\theta^1\text{Ori C}$ (Kristensen et al. 2003). Ionizing radiation has cleared away the diffuse gas and is now slowly eating its way through the denser clumps of gas remaining. Thus the line of WRVs along the eastern edge of Peak 1 may be the relic of a denser region that existed in the original molecular cloud. Whilst the brightness of the H_2 emission cannot be reconciled with a face-on PDR (see sect. 3.2), PDR emission may be enhanced locally through a geometry originally proposed in Field et al. (1994). In this model, a choppy surface of H_2 yields chance lines-of-sight with high column density. This is consistent with the broken up appearance of 2/3 of the features in this zone, mentioned in sect. 4.3.

If we consider only those WRVs lying in the band of width $2.5''$ between points P and Q in fig. 4, a further possibility is that these may be associated with an outflow in the plane of the sky from IRc9 (00726 in table 1 and fig. 17). IRc9 is located $\sim 2''$ from the centre of this band. Smith & Bally (2005) show that IRc9 is a YSO possessing a clearly defined disk. The major axis of the disk is oriented at right-angles to the WRV band which

suggests that WRVs in the band could represent a highly collimated outflow in the plane of the sky from IRc9. In sect. 4.3 we found that there was a significant overrepresentation of WRVs in Peak 1. If the analysis is repeated but without including the WRVs in the band, a significant overrepresentation of WRVs in Peak 1 is still found: based on the same model used in sect. 4.3 the expected number of WRVs in Peak 1 is ~ 12 while 32 WRVs are actually observed. Thus a significant discrepancy remains.

6. The outflow zone, Region B

6.1. The geometry of the region: radio observations and the present data

An outflow in Region B has previously been identified in radio-observations involving both proper motions and radial velocity measurements of H_2O , OH and SiO masers and thermal emission in SiO ($v=0$) and NH_3 . Evidence of shocked gas within the flow is provided through observations of emission from high rotational states of SO, SO_2 , HCN, where data are reviewed in Genzel & Stutzki (1989). The outflow has also been identified in subsequent observations reported in Wright et al. (1992, 1996) in data involving 16 molecular species, in particular SO and SO_2 (Wright et al. 1996). The outflow is associated with source I whose location is given in Fig. 19.

The expansion velocity associated with the above-mentioned outflow in Region B on the basis of radio observations was found to be $18 \pm 2 \text{ km s}^{-1}$ (Genzel et al. 1981). The data of Genzel et al. (1981) showed a flow extending $\sim 20''$ SW of the BN-IRc2 region, which is very similar to the SW extent of the H_2 emission recorded here. Genzel et al. (1981) also note, through their observations of numerous objects at closely similar velocity, that the flow appears to have been stable for $\gtrsim 3000$ years. This would seem to preclude the scenarios discussed in Shuping et al. (2004) in which source I may be the origin of both of the major outflows in this region, through unstable behaviour, such as flipping of the orientation of the outflow.

Menten & Reid (1995) performed SiO maser observations of the centre of the region around source I, extending over ~ 50 AU ($0.11''$), and found both blue- and red-shifted flows, with the blue-shifted component showing a v_{lsr} between -13.0 and -6.2 km s^{-1} corresponding to a blue-shifted flow relative to the ambient gas of between 25 and $18 \pm 6 \text{ km s}^{-1}$, taking into account the uncertainty in the v_{lsr} . The centre of the SiO maser emission was found to be located at the position of source I. The same spatial relationship of SiO masers to source I is recorded in Doeleman et al. (1999). Further recent SiO observations covered an inner area of $\leq 2''$ diameter (900 AU) and involved both SiO maser and non-maser emission, the latter in $v=0$, and maser emission in H_2O , including proper motion studies (Greenhill et al. 2004a). As in Menten & Reid (1995), the expansion centre of these motions was found

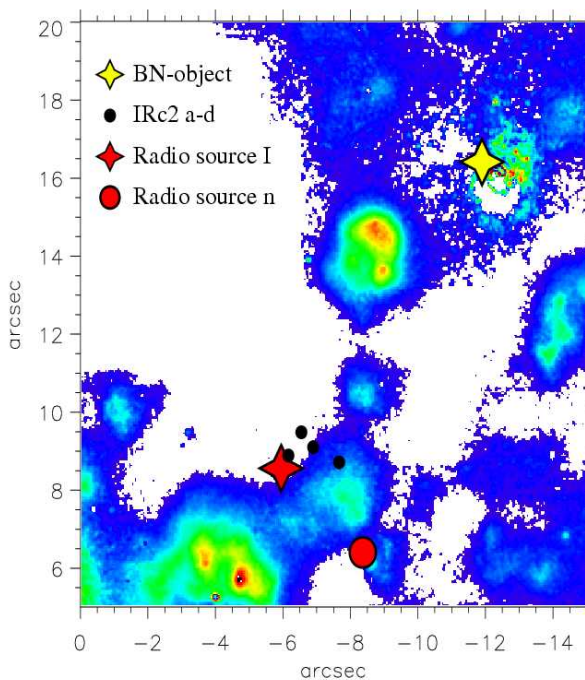


Figure 19. The positions of BN, radio source I, radio source n and IRc2 a-d, superimposed on velocity integrated emission in the $v=1-0$ H_2 $\text{S}(1)$ line.

to be coincident with source I, in this case to within 30 mas (~ 15 AU). Radio source n (hereafter simply source n, see Fig. 19) a few arcseconds from source I is also significant. From the observations of Genzel et al. (1981) and Menten & Reid (1995) source n is found at the centre of expansion of a shell of H_2O masers, perhaps constituting an independent outflow zone (Shuping et al. 2004).

Our present observations measure gas motions relative to the ambient surrounding gas and therefore may also be interpreted as a radial component of an expansion velocity. The expansion velocity of 18 ± 2 km s^{-1} derived from the observations of Genzel et al. (1981) matches accurately the mean velocity of -18 km s^{-1} observed here for the hot H_2 in Region B: see Fig. 5. The velocities measured in this work are also consistent with data in Menten & Reid (1995) and Wright et al. (1996).

The much debated issue of the origin of large scale outflows in OMC1, examined in detail for example in Menten & Reid (1995) and elsewhere, has recently achieved a new perspective with high spatial resolution ($0.3\text{--}0.5''$) IR measurements in Shuping et al. (2004) and Greenhill et al. (2004b). These observations show that there are a number of potential YSO candidates buried within a zone in the north-east of Region B. IRc2 was long believed to be the main power source in OMC1 and the source of the outflow activity in the region. However these and other high resolution observations (Douglas et al. 1993) have resolved IRc2 into several individual sources. These may or may not be self-luminous (Shuping et al. 2004). At all events

the current most likely candidates for outflow sources are sources I and n.

The positions of sources are shown in Fig. 19. Source I ($-5.95''$ E, $8.56''$ N), is a deeply buried O-star (Menten & Reid 1995; Greenhill et al. 2004a). It is the most luminous source in the hot core of OMC1 with a luminosity of 5×10^3 to 10^4 L_\odot (Menten & Reid 1995; Beuther et al. 2004, and see sect. 6.2), compared for example to $\sim 2500 \text{ L}_\odot$ for the BN-object (Gezari et al. 1998) or $\sim 2000 \text{ L}_\odot$ estimated for source n (Greenhill et al. 2004b). Source I is obscured in the infrared and cannot be detected at wavelengths as long as $22 \mu\text{m}$ (Greenhill et al. 2004b). Source n (Greenhill et al. 2004b) is located at $-8.35''$ E, $6.40''$ N and according to Shuping et al. (2004) may give rise to an outflow in this region (see above and sect. 6.3).

Based on their data for SiO and H_2O emission around source I, Greenhill et al. (2004a) proposed a model with an accretion disk and a wide angle outflow pointing NE-SW with an opening angle of $\sim 90^\circ$. This model replaces that of Greenhill et al. (1998). The morphology of the outflow from source I, newly proposed in Greenhill et al. (2004a), is shown in Fig. 20, lower left panel.

The axis of the outflow from source I passes through a region where we find a striking H_2 emission feature. Velocity data for this zone is shown in the upper right hand frame of Fig. 20. Three fast jets (flows no. B-7, B-9, B-10: see Table A.3) are seen impinging on the surrounding medium. A VLT image of the same area (Lacombe et al. 2004) is shown in the lower right-hand frame of Fig. 20. The model of the outflow from source I is superimposed upon it, to show the spatial relationship, where the accuracy of the relative positions is $\sim 0.2''$. The position of the maximum brightness of this outflow region, measured in H_2 , is $1.84''$ W and $0.96''$ S of source I. The appearance of the H_2 emission in this region suggests that this is a zone where the radio-detected outflow bursts through the dense gas surrounding source I. Thus our observations show the IR counterpart of the O-star outflow, hitherto only observed at radio-wavelengths.

The model of Greenhill et al. (2004a) of the outflow from Source I is of an O-star with an edge-on disk and a wide-angle (90°) bipolar outflow in the plane of the sky. This begs the question of why no H_2 emission is observed as part of the outflow to the NE of source I. We would suggest that the flow axis may in fact tip out of the plane of the sky by $\lesssim 45^\circ$. Flows would then tend to be rendered invisible through dust obscuration in this very dense zone. Moreover, Greenhill et al. (2004a) observe a substantial overlap of H_2O and SiO masers along the line-of-sight. However these two molecular masers trace different gas densities and temperatures, and as Greenhill et al. (2004a) note should not be found within the same mass of gas. H_2O masers may have associated kinetic temperature of 200 to 2000 K, with a preference for temperatures around 600 K, and densities of no more than a few $\times 10^9 \text{ cm}^{-3}$ but most likely with densities $< 10^9 \text{ cm}^{-3}$ (Yates et al. 1997). SiO masers require SiO to remain in the gas phase, with associated temperatures of > 1500 K and densities of 10^{10} cm^{-3}

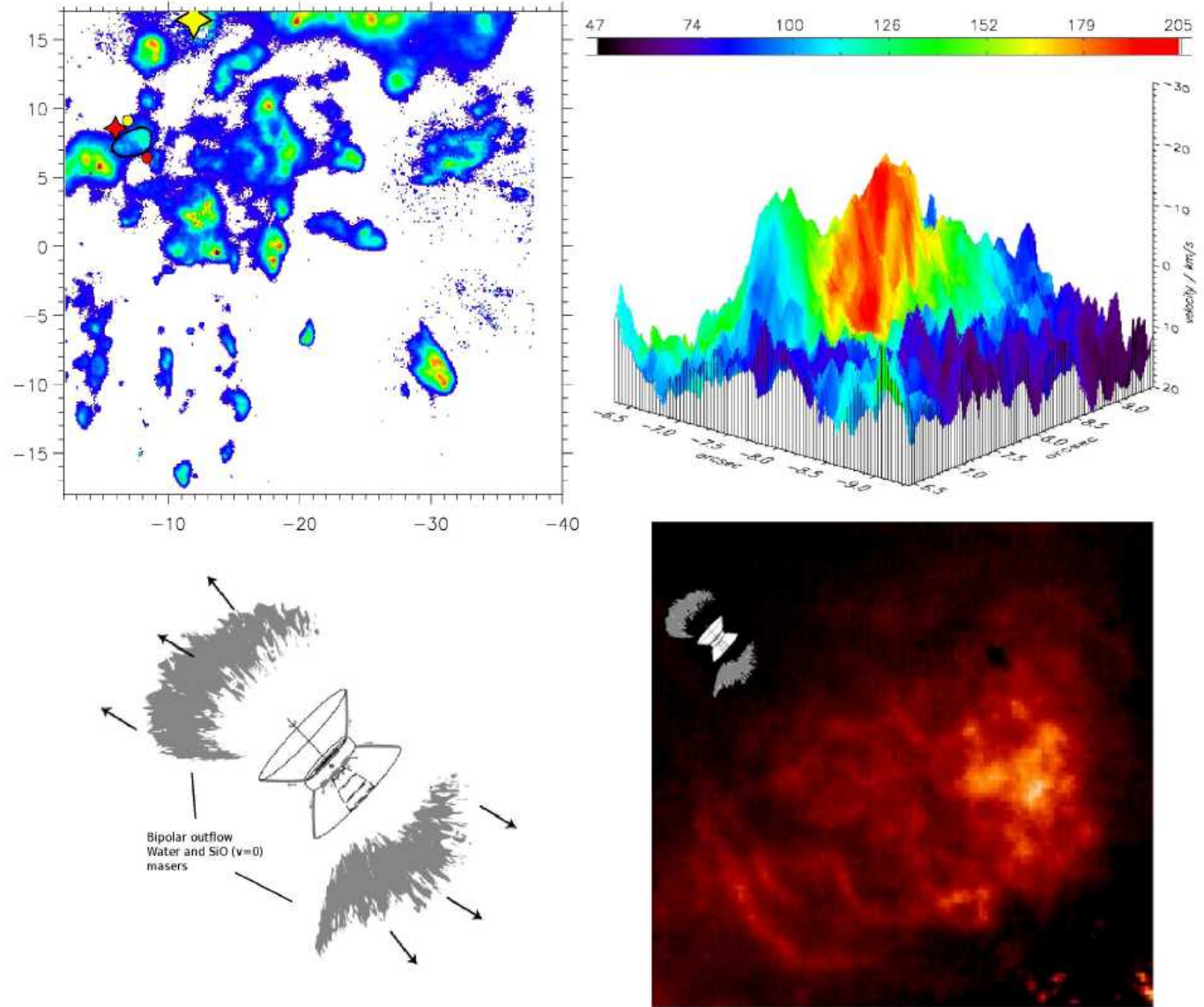


Figure 20. Source I. **Top left:** Region B recorded in the $v=1-0$ $S(1)$ line of H_2 . The yellow star shows the position of BN and the red star shows the position of source I. The red circle is source n, and the yellow circle is IRc2 d (compare to Fig. 19). The black outline shows the position of the H_2 emission feature shown in the right hand panels. **Bottom left:** the geometry of the wide-angle outflow from source I taken from Greenhill et al. (2004a). **Bottom right:** VLT NACO image (Lacombe et al. 2004) of the outflow region (the "fireball") just SW of source I, outlined in black in the top left panel. The inset shows that the outflow from source I (not to scale) points directly at this region. **Top right:** velocity structure of the fireball, showing three fast jets impinging on the medium (flows no. B-7, B-9, B-10: see Table A.3).

(Doel et al. 1995; Humphreys et al. 1996). If, however, the outflow cone has a significant component in the line-of-sight, as we suggest here, this discrepancy may be resolved: the H_2O masers lie further from the O-star than the SiO masers, but overlap in the line of sight. Further, blue-shifted flows are observed to the north of Source I. This is consistent with an outflow originating from source I, but tipped out of the plane as we suggest. This is illustrated in Fig. 21 – described in more detail below – where any material to the left of the line-of-sight through source

I would effectively appear as blue-shifted material to the north of source I.

In conclusion we agree with Greenhill et al. (2004a) that the direction of the outflow in the plane of the sky is NE-SW. Following the result of sect. 5.1, the position angle of the axis of the cone of the outflow from source I is $\sim 240^\circ \pm 10^\circ$. We suggest however that the flow, rather than lying in the plane of the sky, lies at an angle of as much as 45° to this plane.

A schematic diagram of the region, not to scale, based upon this model, may be found in Fig. 21. This shows the

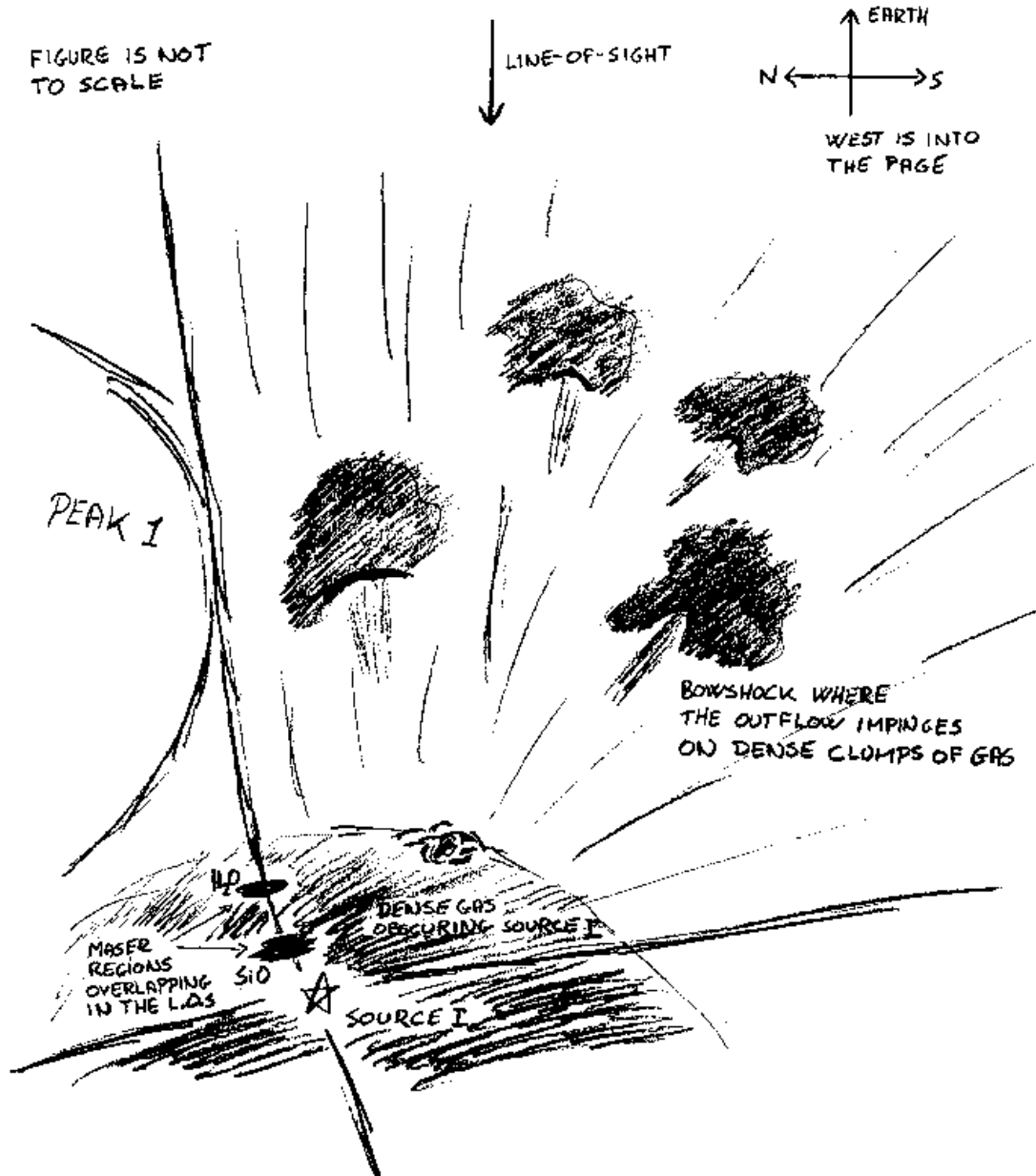


Figure 21. The outflow from source I, showing the appearance of the outflow and its relationship to other objects in Region B, seen at right-angles to the line-of-sight from a vantage point in Peak 2 looking towards the west.

region as if observed from right-angles to the line-of-sight, from a position in Peak 2, looking west. Starting from source I at the base of the diagram, first SiO and then H₂O masing regions, overlapping in the line-of-sight, are found in the dense gas close to source I. Moving further from the O-star, the outflow breaks through the dense gas and dust surrounding source I, generating H₂ emission features such as that shown in Fig. 20 and, moving still further, other blue-shifted features shown in Fig. 4 and listed in Table A.3.

The model proposed above requires that the directions of flows of H₂ emitting regions should show asymmetry in the NE-SW direction. Referring to Fig. 4 and Fig. 16, the star diagram for Region B in the upper left panel shows

a 3:1 anisotropy about a dividing line running roughly perpendicular to the outflow direction. In this connection, recollect that the absolute direction of the flow, $\pm 180^\circ$ is not determined, as noted earlier. The only additional assumption at this juncture is that one or other model on which the flow direction is based is dominant, see sect. 5.1.

6.2. Physical properties of the outflow source

This section considers some of the governing parameters of the O-star associated with source I and with region B. Greenhill et al. (2004b) found that source I could not be detected at 22 μ m. They concluded that the optical depth at 22 μ m must be >300 . Using the relationship between

extinction and wavelength given in Rosenthal et al. (2000), the NIR optical depth will then be >570 . This implies that the column density of H_2 is $>1.5 \times 10^{25} \text{ cm}^{-2}$. This is comparable with the figure of $\leq 8.5 \times 10^{24} \text{ cm}^{-2}$ estimated in Beuther et al. (2004). Depending on the average gas density around the obscured O-star, this object must be buried several arcseconds within OMC1. For example if the average density is 10^9 cm^{-3} , the O-star is buried to a depth of $2''$ and the mass of gas surrounding the O-star is 9 M_\odot . This is comparable with the estimate of the mass of the O-star itself of $\leq 10 \text{ M}_\odot$ in Beuther et al. (2004) or the figure of $10\text{-}20 \text{ M}_\odot$ given in Shuping et al. (2004). These masses are consistent with a luminosity of a few thousand to $\sim 10^4 \text{ L}_\odot$, consistent also with Menten & Reid (1995). The most recent estimate places the luminosity of source I at $\sim 5 \times 10^3 \text{ L}_\odot$ (Beuther et al. 2006, 2004).

The mass outflow rate in Region B may be estimated as follows. Typical gas densities in the H_2 clumps in Region B have been investigated in detail in Kristensen et al. (2006) and post-shock values range between 10^6 to 10^7 cm^{-3} , equivalent to an average density of $\sim 10^{-17} \text{ g cm}^{-3}$. Assuming a continuous outflow and a measured velocity of 18 km s^{-1} , this represents a mass flux of $2 \times 10^{-11} \text{ g cm}^{-2} \text{ s}^{-1}$. The total area in the plane of the sky covered by the excited H_2 may be estimated by using a total area for each clump given by the area around each flow where the emission is $\geq 50\%$ of the maximum brightness of the flow. The total area is found to be $\sim 5 \times 10^{33} \text{ cm}^2$, giving a mass flow of $\sim 1.5 \times 10^{-3} \text{ M}_\odot \text{ yr}^{-1}$. Including the red-shifted part of a bipolar outflow, this gives a total outflow rate of $\sim 3 \times 10^{-3} \text{ M}_\odot \text{ yr}^{-1}$. Since only excited gas has been included this is a lower limit. This figure for the outflow rate is comparable to estimates given in Shepherd (2005) for stars of the luminosity associated with source I.

An independent estimate of the outflow rate may also be performed. If the luminosity of the source is accretion luminosity and the surface temperature is (say) 1500 K , typical of a protostar, then the stellar radius is $\sim 5 \text{ AU}$, given the figure of $5 \times 10^3 \text{ L}_\odot$. The mass infall rate is then $0.02 \text{ M}_\odot \text{ yr}^{-1}$. For low mass stars the outflow rate is generally $\sim 10\%$ of the infall rate (Richer et al. 2000). If the same proportion is adopted for the case of this massive star, the result is a mass outflow rate which is essentially the same as that which has been estimated from our observations. The corresponding outflow momentum rate is $\sim 0.05 \text{ M}_\odot \text{ yr}^{-1} \text{ km s}^{-1}$ and mechanical luminosity is $\sim 80 \text{ L}_\odot$. These values are typical of a late-type O-star or early-type B-star (Shepherd 2005). Together these characteristic properties combine to make a consistent picture of an outflow from source I where this source is a massive and very young star.

6.3. Source n

As already noted, source n (Menten & Reid 1995) is another major power source in the region, in addition to

source I and BN. Source I and n lie on a line running NE-SW as shown in fig. 19. Therefore source n is also located on the axis of the low-velocity outflow in Region B. Furthermore Shuping et al. (2004) and Greenhill et al. (2004b), see also Beuther et al. (2004), have made observations which suggest the presence of a disk around source n with the rotation axis aligned with the low-velocity outflow. Thus source n, which is a possible centre of expansion of numerous H_2O masers in the vicinity (Genzel et al. 1981; Menten & Reid 1995), may be the source of or may contribute to the low-velocity outflow in Region B. However, at present source I would seem the clearer candidate following the observations of Greenhill et al. (2004a) and also the fact that source n may have a relatively low luminosity of $\sim 2000 \text{ L}_\odot$ (Greenhill et al. 2004b) compared to source I.

7. Conclusions

The major conclusions of this study using GrIF data for the central region of Orion OMC1 may be summarised as follows.

- (i) 193 distinct bright H_2 emission features in the $v=1\text{-}0 \text{ S}(1)$ line have been identified. 67% of these show clear radial velocity structure with well defined features of greater than 5 km s^{-1} , indicating that the emission is generated by shocks in the medium.
- (ii) There are equal numbers of flows in Peaks 1 and 2, implying a greater concentration of activity in Peak 2 which is less than half the size of Peak 1. Flows are found to be grouped much more tightly in Peak 2 than in Peak 1. Blue shifted flows are somewhat favoured over red-shifted, presumably due to dust obscuration. No velocities exceed $35\text{-}40 \text{ km s}^{-1}$, consistent with the upper limit for the propagation of C-type shocks in dense media.
- (iii) In a distinct zone, Region B, lying south of Peak 1 and west of peak 2, all flows are blue-shifted, with an average velocity of $-18 \pm 8 \text{ km s}^{-1}$.
- (iv) Weak radial velocity features (WRVs) with radial velocities $< 5 \text{ km s}^{-1}$ are strongly concentrated in Peak 1, and a band of such structures has been identified in a NE-SW direction across Peak 1. In this band, 2/3 of the structures show a broken-up morphology, not seen elsewhere, which may arise from a major photodissociation contribution to the emission through geometrical projection effects. This band of structures may also be a further manifestation of an outburst from the BN-IRc2 region about 1000 years ago which created the bullets or fingers lying further to the NW.
- (v) Spatial correlation between maximum brightness of H_2 emission and maximum velocity reveals deviations typically of $\leq 0.6''$. These deviations may be used to estimate the orientation of flows, or shocks, in the plane of

the sky - but not their absolute direction, that is, whether they are travelling north or south, say. Orientations are found to be random in Peak 2 and with some clear preference for a SE-NW direction in Peak 1, but show a strong preference for a NE-SW orientation in Region B.

(vi) In Paper I it was noted that potential low mass star forming zones, identified through the presence of energetic flows in OMC1, showed higher densities and correspondingly higher energy flux, and are altogether less simply structured than more conventional Class 0 or 1 low mass isolated star formation regions. Here we identify a large number of zones which show similar characteristics to those discussed in Paper I. Data point in particular to the close physical association of numerous strong H₂ emission features. It would seem likely that these associations represent sites of multiple star formation characterised by episodic outbursts of activity creating several outflows in different directions.

(vii) The most striking feature of the results is the blue-shifted outflow in Region B. This is the infrared counterpart to the outflow associated with the very young O-star, source I, a radio source with associated SiO and H₂O masers and non-maser emission in numerous molecules. Radio data show the presence of a blue-shifted flow, part of a general expansion with an average velocity of $18 \pm 6 \text{ km s}^{-1}$, in agreement with our value of $-18 \pm 8 \text{ km s}^{-1}$.

(viii) There is a remarkable feature in the H₂ emission data with strong velocity components. On the basis of a VLT image, this is suggestive of a region in which a flow has burst through the material of OMC1 from behind, originating in source I and sending shock waves through the medium. The axis of the radio outflow from source I passes through this object. These and other data lead us to conclude that source I is a major progenitor of activity in OMC1 and in particular of the outflow in region B.

(ix) There remain several extraordinary objects in the field whose nature we do not comprehend. For example there is a structure, $3'' \times 3''$, Table A.2, object 2-32 and 2-34 in Peak 2, which is the only clump of emission in the entire field with v_{lsr} consistently around $>40 \text{ km s}^{-1}$ (shown in Fig. 4 of Gustafsson et al. 2006). The origin of such an energetic object is unknown.

In conclusion, the GriF data with its associated high spatial and velocity resolution provide information which opens a new window on OMC1 and presents a new perspective on the star-forming activity for both massive and low mass stars. Data have very recently been obtained for OMC1 using the VLT with adaptive optics and Fabry-Perot interferometry in the $v=1-0$ S(1), S(0) and the $v=2-1$ S(1) lines. Shock structures seen in these 3 lines will constrain the physical conditions strongly in

star forming zones in OMC1. The chief lack at present is of shock models which contain both detailed chemistry, essential for C-type shocks, and also the geometry, for example of bow shocks. Models are under development and will be necessary to settle such basic questions as the relative physical disposition of the location of the maximum brightness and maximum velocity in H₂ emission features.

Acknowledgements. HDN, MG and DF would like to acknowledge the support of the Aarhus Centre for Atomic Physics (ACAP), funded by the Danish Basic Research Foundation. HDN and MG would also like to acknowledge financial support from the Instrument Centre for Danish Astrophysics (IDA), funded by the Danish National Science Committee (SNF, now FNU). JLL would like to acknowledge the support of the PCMI National Program, funded by the French Centre National de la Recherche Scientifique (CNRS). We also wish to thank the Directors and Staff of CFHT and of the VLT for making possible observations reported in this paper and for the assistance rendered by E. Le Coarer (Observatoire de Grenoble) in obtaining GriF data. We also wish to thank G. Pineau des Forêts and Lars E. Kristensen for valuable discussions about the nature of shocks. Our thanks are also due to the referee for many helpful comments, and to whom we owe, among other items, the suggestion that we include details of protostellar candidates and the model that the outflow from IRc9 may be the source of some of the anomalous objects found in our field.

References

- Allen, D. A. & Burton, M. G. 1993, Nature, 363, 54
- Axon, D. J. & Taylor, K. 1984, MNRAS, 207, 241
- Bally, J., O'Dell, C. R., & McCaughrean, M. J. 2000, AJ, 119, 2919
- Bate, M. R., Bonnell, I. A., & Bromm, V. 2003, MNRAS, 339, 577
- Beckwith, S., Persson, S. E., Neugebauer, G., & Becklin, E. E. 1978, ApJ, 223, 464
- Beuther, H., Zhang, Q., Greenhill, L. J., et al. 2004, ApJ, 616, L31
- Beuther, H., Zhang, Q., Reid, M. J., et al. 2006, ApJ, 636, 323
- Bontemps, S., Andre, P., Terebey, S., & Cabrit, S. 1996, A&A, 311, 858
- Bragg, S. L., Smith, W. H., & Brault, J. W. 1982, ApJ, 263, 999
- Burton, M. G. 1997, in ASP Conf. Ser. 121: IAU Colloq. 163: Accretion Phenomena and Related Outflows, 571–574
- Chen, H., Bally, J., O'Dell, C. R., et al. 1998, ApJ, 492, L173+
- Chrysostomou, A., Burton, M. G., Axon, D. J., et al. 1997, MNRAS, 289, 605
- Chrysostomou, A., Gledhill, T. M., Ménard, F., et al. 2000, MNRAS, 312, 103
- Clénet, Y., Le Coarer, E., Joncas, G., et al. 2002, PASP, 114, 563
- Davis, C. J., Ray, T. P., Desroches, L., & Aspin, C. 2001, MNRAS, 326, 524

Delgado-Donate, E. J., Clarke, C. J., Bate, M. R., & Hodgkin, S. T. 2004, MNRAS, 351, 617

Doel, R. C., Gray, M. D., Humphreys, E. M. L., Braithwaite, M. F., & Field, D. 1995, A&A, 302, 797

Doeleman, S. S., Lonsdale, C. J., Kondratko, P. T., & Predmore, C. R. 2004, ApJ, 607, 361

Doeleman, S. S., Lonsdale, C. J., & Pelkey, S. 1999, ApJ, 510, L55

Doi, T., O'Dell, C. R., & Hartigan, P. 2002, AJ, 124, 445

Dougados, C., Lena, P., Ridgway, S. T., Christou, J. C., & Probst, R. G. 1993, ApJ, 406, 112

Feigelson, E. D., Broos, P., Gaffney, J. A., et al. 2002, ApJ, 574, 258

Ferland, G. J. 2001, PASP, 113, 41

Field, D., Gerin, M., Leach, S., et al. 1994, A&A, 286, 909

Flower, D. R., Le Bourlot, J., Pineau des Forêts, G., & Cabrit, S. 2003, MNRAS, 341, 70

Garmire, G., Feigelson, E. D., Broos, P., et al. 2000, AJ, 120, 1426

Genzel, R., Reid, M. J., Moran, J. M., & Downes, D. 1981, ApJ, 244, 884

Genzel, R. & Stutzki, J. 1989, ARA&A, 27, 41

Getman, K. V., Flaccomio, E., Broos, P. S., et al. 2005, ApJS, 160, 319

Gezari, D. Y., Backman, D. E., & Werner, M. W. 1998, ApJ, 509, 283

Greenhill, L. J., Chandler, C. J., Reid, M. J., et al. 2004a, in IAU Symposium 221

Greenhill, L. J., Gezari, D. Y., Danchi, W. C., et al. 2004b, ApJ, 605, L57

Greenhill, L. J., Gwinn, C. R., Schwartz, C., Moran, J. M., & Diamond, P. J. 1998, Nature, 396, 650

Grosso, N., Feigelson, E. D., Getman, K. V., et al. 2005, ArXiv Astrophysics e-prints, astro-ph/0504204

Gustafsson, M., Field, D., Lemaire, J. L., & Pijpers, F. 2006, A&A, 445, 601

Gustafsson, M., Kristensen, L. E., Clénet, Y., et al. 2003, A&A, 411, 437

Hartigan, P. 1989, ApJ, 339, 987

Henney, W. J. & O'Dell, C. R. 1999, AJ, 118, 2350

Hillenbrand, L. A. 1997, AJ, 113, 1733

Humphreys, E. M. L., Gray, M. D., Yates, J. A., et al. 1996, MNRAS, 282, 1359

Kenyon, S. J. & Hartmann, L. 1995, ApJS, 101, 117

Kristensen, L. E., Gustafsson, M., Field, D., et al. 2003, A&A, 412, 727

Kristensen, L. E., Ravkilde, T. L., Field, D., Lemaire, J. L., & Pineau des Forêts, G. 2006, in preparation.

Lacombe, F., Gendron, E., Rouan, D., et al. 2004, A&A, 417, L5

Lada, C. J., Muench, A. A., Haisch, K. E., et al. 2000, AJ, 120, 3162

Lada, C. J., Muench, A. A., Lada, E. A., & Alves, J. F. 2004, AJ, 128, 1254

Larson, R. B. 2003, Reports of Progress in Physics, 66, 1651

Le Bourlot, J., Pineau des Forêts, G., Flower, D. R., & Cabrit, S. 2002, MNRAS, 332, 985

Lee, J.-K. & Burton, M. G. 2000, MNRAS, 315, 11

McCaughrean, M. J. & Mac Low, M. 1997, AJ, 113, 391

Menten, K. M. & Reid, M. J. 1995, ApJ, 445, L157

Muench, A. A., Lada, E. A., Lada, C. J., & Alves, J. 2002, ApJ, 573, 366

O'Dell, C. R. 2001, ARA&A, 39, 99

O'Dell, C. R. & Doi, T. 2003, AJ, 125, 277

O'Dell, C. R., Hartigan, P., Lane, W. M., et al. 1997, AJ, 114, 730

Pogge, R. W., Owen, J. M., & Atwood, B. 1992, ApJ, 399, 147

Pudritz, R. E. 2002, Science, 295, 68

Raga, A. & Cabrit, S. 1993, A&A, 278, 267

Richer, J. S., Shepherd, D. S., Cabrit, S., Bachiller, R., & Churchwell, E. 2000, Protostars and Planets IV, 867

Rigaut, F., Salmon, D., Arsenault, R., et al. 1998, PASP, 110, 152

Rosenthal, D., Bertoldi, F., & Drapatz, S. 2000, A&A, 356, 705

Salas, L., Rosado, M., Cruz-González, I., et al. 1999, ApJ, 511, 822

Schild, H., Miller, S., & Tennyson, J. 1997, A&A, 318, 608

Schultz, A. S. B., Colgan, S. W. J., Erickson, E. F., et al. 1999, ApJ, 511, 282

Shepherd, D. 2005, in IAU Symposium 227, 237–246

Shuping, R. Y., Morris, M., & Bally, J. 2004, AJ, 128, 363

Smith, N. & Bally, J. 2005, ApJ, 622, L65

Störzer, H. & Hollenbach, D. 1999, ApJ, 515, 669

Stanke, T. 2000, Ph.D. Thesis

Stolovy, S. R., Burton, M. G., Erickson, E. F., et al. 1998, ApJ, 492, L151

Stone, J. M., Xu, J., & Mundy, L. G. 1995, Nature, 377, 315

Takami, M., Usuda, T., Sugai, H., et al. 2002, ApJ, 566, 910

Tan, J. C. 2004, in ASP Conf. Ser. 323: Star Formation in the Interstellar Medium: In Honor of David Hollenbach, 249

van Altena, W. F., Lee, J. T., Lee, J.-F., Lu, P. K., & Upgren, A. R. 1988, AJ, 95, 1744

Vannier, L., Lemaire, J. L., Field, D., et al. 2001, A&A, 366, 651

Wen, Z. & O'Dell, C. R. 1995, ApJ, 438, 784

Wilgenbus, D., Cabrit, S., Pineau des Forêts, G., & Flower, D. R. 2000, A&A, 356, 1010

Wright, M., Sandell, G., Wilner, D. J., & Plambeck, R. L. 1992, ApJ, 393, 225

Wright, M. C. H., Plambeck, R. L., & Wilner, D. J. 1996, ApJ, 469, 216

Yates, J. A., Field, D., & Gray, M. D. 1997, MNRAS, 285, 303

Appendix A: Tables

Table A.1. Features identified in OMC1 in Peak 1. Data are sorted by the east-coordinate of the maximum in brightness. Column **1** labels each feature and columns **2–5** show the position in the plane of the sky of the maxima in brightness and velocity for each of the features. Positions are measured in arcseconds east and north of the star TCC0016 ($05^{\text{h}}35^{\text{m}}14^{\text{s}}.91$, $-05^{\circ}22'39.31$ (J2000)). Where no coordinates are given for a maximum in velocity, no well-defined peak in the velocity was found nearby. Columns **6** shows the velocity of the gas surrounding each feature expressed as v_{lsr} . Column **7** shows the maximum velocity of the flow relative to this local background velocity (see sect. 3.1). Column **8** contains the maximum brightness of each feature per 400 s exposure. Column **9** shows the position angle for each flow, measured east of north (i.e. counter-clockwise), see sect. 5.2. A dash indicates that the object is a weak radial velocity region (WRV) and 'no p.a.' indicates a displacement between maximum velocity and brightness of $<0.25''$. A star (*) marks flows where the morphology of the emission clearly indicates the absolute direction of the flow (see sect. 5.1): these are only found in Table A.3. Column **10** gives the displacement in the plane of the sky between the observed maxima in brightness and velocity for each feature. A summary of the data can be seen in Fig. 4.

No.	Flows in Peak 1								
	Coordinates of maxima				velocity of surroundings km s ⁻¹	flow velocity km s ⁻¹	maximum brightness counts	position angle degrees	displacement arcsec
	Brightness		Velocity						
	E	N	E	N	km s ⁻¹	km s ⁻¹	counts	degrees	arcsec
1-1	-3.61	43.58	—	—	17	—	204	—	—
1-2	-7.14	43.68	-7.11	43.12	16	-6	207	356	0.6
1-3	-7.77	22.61	-7.60	22.54	8	-14	421	no p.a.	0.2
1-4	-8.51	46.87	-8.47	47.39	20	9	398	184	0.5
1-5	-9.48	47.28	—	—	20	—	368	—	—
1-6	-9.52	27.09	—	—	8	—	302	—	—
1-7	-9.90	44.94	—	—	21	—	302	—	—
1-8	-10.22	42.46	-10.05	41.90	21	7	264	343	0.6
1-9	-10.26	46.38	—	—	20	—	366	—	—
1-10	-12.18	29.89	-13.06	30.73	13	-16	227	134	1.2
1-11	-12.36	36.85	—	—	16	—	224	—	—
1-12	-12.39	28.59	-11.94	28.77	13	19	196	249	0.5
1-13	-13.16	41.16	—	—	17	—	290	—	—
1-14	-13.61	29.05	—	—	13	—	229	—	—
1-15	-13.86	22.61	-13.48	22.43	6	-28	187	294	0.4
1-16	-14.18	40.95	—	—	18	—	328	—	—
1-17	-14.91	46.72	—	—	22	—	259	—	—
1-18	-15.19	42.98	-15.54	42.84	14	-9	412	68	0.4
1-19	-15.30	38.53	—	—	18	—	323	—	—
1-20	-15.75	32.80	-16.27	32.72	6	-7	308	82	0.5
1-21	-15.86	30.80	-15.54	29.47	10	13	324	347	1.4
1-22	-16.49	37.66	—	—	14	—	271	—	—
1-23	-17.50	43.82	—	—	12	—	426	—	—
1-24	-17.67	21.25	-17.53	21.52	11	-10	236	207	0.3
1-25	-17.75	36.51	—	—	11	—	410	—	—
1-26	-18.48	35.49	-18.41	34.76	9	-9	543	355	0.7
1-27	-18.51	32.72	—	—	8	—	445	—	—
1-28	-18.59	23.34	-17.64	23.76	10	-29	227	246	1.0
1-29	-18.69	42.70	—	—	14	—	409	—	—
1-30	-18.76	30.38	-18.83	29.75	4	-8	362	6	0.6
1-31	-19.25	21.21	—	—	12	—	304	—	—
1-32	-19.99	25.93	—	—	9	—	257	—	—
1-33	-20.37	28.67	-20.12	28.45	8	-40	316	311	0.3
1-34	-20.58	35.98	-20.26	35.00	13	10	483	342	1.0
1-35	-20.61	42.24	—	—	16	—	286	—	—
1-36	-20.68	30.14	-20.97	29.30	8	-17	536	18	0.9
1-37	-21.00	32.55	—	—	12	—	439	—	—
1-38	-21.21	33.99	-21.14	33.95	12	-8	439	no p.a.	0.1
1-39	-21.49	37.28	-21.07	37.45	14	-9	480	247	0.5
1-40	-21.84	38.64	-21.84	39.87	15	-7	401	180	1.2

Continued on next page

Table A.1. continued.

No.	Coordinates of maxima				velocity of surroundings km s ⁻¹	flow velocity km s ⁻¹	maximum brightness counts	position angle degrees	displacement arcsec
	Brightness		Velocity						
	E	N	E	N					
1-41	-21.88	34.51	—	—	12	—	416	—	—
1-42	-22.01	21.74	—	—	7	—	223	—	—
1-43	-22.23	24.29	-21.88	24.01	11	-9	357	309	0.4
1-44	-22.43	30.24	—	—	10	—	389	—	—
1-45	-22.50	18.48	—	—	7	—	471	—	—
1-46	-22.61	19.92	—	—	6	—	295	—	—
1-47	-23.80	35.21	-23.91	35.14	12	15	332	no p.a.	0.1
1-48	-24.11	37.56	-23.94	36.65	13	-8	329	349	0.9
1-49	-24.33	19.67	-23.98	19.57	10	-14	413	287	0.4
1-50	-24.57	21.03	-24.33	20.79	12	13	271	315	0.3
1-51	-24.82	28.21	—	—	16	—	255	—	—
1-52	-25.48	29.92	-25.55	29.19	14	9	282	5	0.7
1-53	-25.66	18.20	—	—	8	—	278	—	—
1-54	-26.04	35.53	-25.76	35.35	10	-31	349	302	0.3
1-55	-26.53	24.40	—	—	17	—	301	—	—
1-56	-26.60	20.79	-26.28	20.86	8	-5	270	257	0.3
1-57	-26.67	32.13	—	—	14	—	378	—	—
1-58	-27.34	33.32	-26.74	33.39	12	-20	394	263	0.6
1-59	-27.55	20.06	—	—	12	—	334	—	—
1-60	-28.17	34.33	-28.49	33.25	12	19	498	16	1.1
1-61	-29.01	21.52	-28.49	21.49	8	-32	293	274	0.5
1-62	-29.68	38.92	-29.51	38.81	19	-8	296	no p.a.	0.2
1-63	-29.68	23.66	—	—	10	—	260	—	—
1-64	-30.73	25.31	-31.11	25.66	15	8	257	132	0.5
1-65	-30.84	22.50	—	—	11	—	276	—	—
1-66	-31.50	20.75	—	—	13	—	335	—	—
1-67	-31.89	37.62	—	—	26	—	235	—	—
1-68	-31.99	31.57	-31.92	31.11	17	-13	266	351	0.5
1-69	-32.24	25.90	—	—	18	—	257	—	—
1-70	-32.69	24.75	—	—	18	—	251	—	—
1-71	-33.39	33.74	—	—	28	—	241	—	—
1-72	-33.78	27.34	-34.79	27.23	20	15	268	84	1.0
1-73	-35.67	39.24	-35.35	38.88	18	-11	270	318	0.5
1-74	-35.84	35.07	—	—	27	—	438	—	—
1-75	-36.22	28.70	-36.92	28.63	23	-16	178	84	0.7
1-76	-36.65	32.97	-35.74	32.65	22	-16	228	289	1.0
1-77	-37.28	21.39	—	—	18	—	235	—	—
1-78	-37.38	24.29	—	—	22	—	236	—	—
1-79	-37.45	32.97	—	—	24	—	263	—	—
1-80	-37.73	23.24	—	—	19	—	237	—	—
1-81	-38.88	32.94	-39.94	32.83	24	7	350	84	1.1
1-82	-39.17	25.83	—	—	22	—	296	—	—
1-83	-40.60	22.19	—	—	18	—	230	—	—
1-84	-40.95	24.29	—	—	16	—	178	—	—
1-85	-44.80	28.94	—	—	21	—	179	—	—
1-86	-45.29	35.46	-45.57	36.12	24	33	178	157	0.7
1-87	-49.17	26.67	—	—	20	—	185	—	—

Table A.2. Flows in Peak 2. For an explanation of each column, see table A.1

No.	Flows in Peak 2									
	Coordinates of maxima				velocity of surroundings	flow velocity	maximum brightness	position angle	displacement	
	Brightness		Velocity							
	E	N	E	N	km s ⁻¹	km s ⁻¹	counts	degrees	arcsec	
2-1	19.39	-6.51	19.25	-6.62	20	14	261	no p.a.	0.2	
2-2	19.00	9.45	19.42	9.41	34	9	233	275	0.4	
2-3	18.59	-5.43	18.73	-5.36	20	9	508	no p.a.	0.2	
2-4	18.38	3.67	17.75	3.71	34	-12	532	93	0.6	
2-5	17.64	-0.74	17.40	-1.23	24	-7	391	27	0.5	
2-6	16.76	8.72	16.84	8.72	41	7	407	no p.a.	0.1	
2-7	16.34	9.73	—	—	41	—	391	—	—	
2-8	16.20	-6.47	16.10	-6.51	29	10	357	no p.a.	0.1	
2-9	16.17	-0.49	16.66	-0.67	24	-9	331	290	0.5	
2-10	15.82	-1.61	15.47	-1.12	24	10	860	144	0.6	
2-11	14.81	6.58	—	—	34	—	287	—	—	
2-12	14.18	9.80	13.90	9.52	40	-8	210	45	0.4	
2-13	13.48	-1.75	—	—	30	—	475	—	—	
2-14	13.37	-0.46	13.51	-0.42	30	7	506	no p.a.	0.1	
2-15	12.91	8.26	—	—	35	—	209	—	—	
2-16	12.36	0.67	—	—	32	—	454	—	—	
2-17	12.22	-2.66	12.36	-3.12	25	-6	244	343	0.5	
2-18	12.15	2.28	—	—	32	—	436	—	—	
2-19	11.65	3.95	11.62	3.88	32	-8	404	no p.a.	0.1	
2-20	10.81	1.23	10.57	1.64	32	11	456	150	0.5	
2-21	10.53	-0.94	10.43	-0.31	32	8	361	171	0.6	
2-22	10.40	8.75	10.81	8.78	34	-7	188	265	0.4	
2-23	10.11	-6.51	—	—	23	—	273	—	—	
2-24	9.66	1.19	9.84	1.01	31	7	349	no p.a.	0.2	
2-25	9.56	2.17	9.38	3.01	31	-10	341	168	0.9	
2-26	8.86	1.78	8.78	1.78	31	-12	370	no p.a.	0.1	
2-27	7.70	6.30	8.12	6.20	30	-7	220	284	0.4	
2-28	7.53	-3.64	—	—	27	—	308	—	—	
2-29	7.07	-1.05	7.03	-1.01	30	-6	335	no p.a.	0.0	
2-30	6.82	-4.69	—	—	26	—	308	—	—	
2-31	6.62	6.86	6.51	6.65	26	-11	182	no p.a.	0.2	
2-32	6.62	2.62	6.72	2.73	30	32	283	no p.a.	0.1	
2-33	6.51	-3.05	6.47	-3.01	28	-6	350	no p.a.	0.0	
2-34	6.30	1.09	6.86	1.33	30	26	310	246	0.6	
2-35	6.30	-0.56	6.30	-0.42	30	15	498	no p.a.	0.1	
2-36	5.95	7.18	5.99	7.24	26	-13	194	no p.a.	0.1	
2-37	5.25	-3.33	5.14	-3.05	32	10	530	159	0.3	
2-38	5.07	-2.77	5.07	-2.24	30	9	323	180	0.5	
2-39	4.80	-8.23	4.24	-7.98	20	-7	205	114	0.6	
2-40	4.62	10.85	4.41	10.95	20	-18	531	no p.a.	0.2	
2-41	3.82	-2.38	3.64	-2.56	31	11	209	no p.a.	0.2	
2-42	3.12	7.66	3.01	7.45	20	-8	305	no p.a.	0.2	
2-43	2.62	0.94	2.66	1.09	20	-7	232	no p.a.	0.1	
2-44	1.92	1.54	1.68	1.58	20	-14	227	no p.a.	0.2	
2-45	1.58	5.28	1.78	4.93	18	6	542	329	0.4	
2-46	1.37	4.03	1.92	3.67	15	4	377	302	0.7	
2-47	0.74	6.05	0.77	6.41	10	-13	372	186	0.4	
2-48	0.14	4.03	-0.42	4.13	10	-8	316	101	0.6	
2-49	-0.07	8.05	-0.14	8.30	12	-15	229	164	0.3	
2-50	-1.05	9.80	—	—	16	—	192	—	—	

Table A.3. Flows in Region B. For an explanation of each column, see table A.1

No.	Flows in Region B									
	Coordinates of maxima				velocity of surroundings	flow velocity	maximum brightness	position angle	displacement	
	Brightness		Velocity							
	E	N	E	N	km s ⁻¹	km s ⁻¹	counts	degrees	arcsec	
B-1	-2.20	5.60	-2.13	5.46	4	-14	240	no p.a.	0.2	
B-2	-3.26	-12.43	-3.61	-12.36	22	-9	174	101	0.4	
B-3	-3.99	6.12	-3.61	6.72	5	-22	348	213	0.7	
B-4	-4.41	-6.05	-4.83	-5.70	22	-8	192	130	0.5	
B-5	-4.66	5.70	-5.57	5.64	5	-34	432	86	0.9	
B-6	-4.93	-8.89	-5.04	-8.89	22	-7	145	no p.a.	0.1	
B-7	-7.77	7.80	-7.95	7.84	7	-28	208	no p.a.	0.2	
B-8	-8.05	13.90	-7.98	13.69	14	-24	255	no p.a.	0.2	
B-9	-8.05	7.66	-7.24	7.32	7	-20	199	293	0.9	
B-10	-8.19	7.32	-7.53	7.00	7	-24	198	295	0.7	
B-11	-8.36	10.29	-8.26	10.36	12	-12	175	no p.a.	0.1	
B-12	-8.68	14.77	-8.78	14.56	14	-21	365	no p.a.	0.2	
B-13	-8.93	13.61	-9.17	13.12	14	-10	343	27	0.5	
B-14	-9.69	-8.75	-9.80	-8.72	27	-13	181	no p.a.	0.1	
B-15	-9.90	-8.19	-9.98	-8.05	27	-14	182	no p.a.	0.2	
B-16	-10.64	-0.49	-10.71	-0.07	13	-13	261	171	0.4	
B-17	-10.99	-16.94	—	—	26	—	231	—	—	
B-18	-11.80	2.13	-11.94	2.38	7	-13	362	150	0.3	
B-19	-11.94	1.58	-11.94	1.54	7	-16	392	no p.a.	0.0	
B-20	-12.32	1.50	-12.49	1.58	7	-18	368	no p.a.	0.2	
B-21	-12.81	2.94	-12.64	2.97	7	-14	365	no p.a.	0.2	
B-22	-13.12	1.92	-13.23	2.00	7	-17	307	no p.a.	0.1	
B-23	-13.69	-0.52	-13.30	0.07	8	-20	531	213*	0.7	
B-24	-13.76	11.44	-13.27	11.86	3	-16	226	229	0.6	
B-25	-14.35	11.90	-13.82	12.01	3	-23	212	259	0.5	
B-26	-14.73	-7.56	-14.45	-6.89	20	-7	178	203*	0.7	
B-27	-15.36	-11.90	-15.36	-11.62	10	-12	200	180	0.3	
B-28	-15.89	12.95	-14.77	13.06	3	-20	216	265	1.1	
B-29	-15.99	7.28	-15.82	7.00	7	-20	163	328	0.3	
B-30	-16.62	13.93	-16.66	13.90	3	-11	167	no p.a.	0.0	
B-31	-16.73	5.99	—	—	7	—	221	—	—	
B-32	-17.29	8.68	-17.15	8.36	8	-20	190	336	0.3	
B-33	-17.57	10.05	-17.57	9.98	4	-17	400	no p.a.	0.1	
B-34	-17.60	7.80	-17.60	7.95	8	-20	206	no p.a.	0.1	
B-35	-17.78	0.17	-17.40	-0.38	10	-26	358	325	0.7	
B-36	-17.95	-1.15	-17.82	-2.13	10	-37	404	352	1.0	
B-37	-18.48	0.00	-17.85	0.38	10	-18	363	239*	0.7	
B-38	-18.73	2.52	-18.51	3.05	15	-14	234	202	0.6	
B-39	-18.76	5.46	—	—	10	—	239	—	—	
B-40	-18.90	7.95	—	—	6	—	281	—	—	
B-41	-19.15	6.65	-19.08	6.72	8	-19	301	no p.a.	0.1	
B-42	-19.67	16.24	-19.84	16.91	7	-19	401	165*	0.7	
B-43	-20.44	-6.76	-20.23	-6.51	7	-36	291	221*	0.3	
B-44	-22.78	7.28	-22.78	7.32	10	-39	173	no p.a.	0.0	
B-45	-23.10	6.05	-22.54	6.12	10	-15	208	263	0.6	
B-46	-23.91	6.34	-23.91	6.34	10	-29	293	no p.a.	0.0	
B-47	-24.75	0.88	-24.85	0.98	8	-20	256	no p.a.	0.1	
B-48	-25.48	16.34	-25.02	16.45	5	-14	356	257	0.5	
B-49	-25.83	0.35	-25.66	0.46	7	-7	188	no p.a.	0.2	
B-50	-27.26	16.49	-27.34	16.45	5	-15	305	no p.a.	0.1	
B-51	-27.55	11.65	-26.99	12.01	12	-19	273	238	0.7	
B-52	-30.03	-8.40	—	—	18	—	379	—	—	
B-53	-30.91	-10.08	—	—	18	—	368	—	—	
B-54	-31.26	5.95	-30.94	6.02	17	-7	314	257	0.3	
B-55	-33.28	7.18	—	—	18	—	249	—	—	
B-56	-33.92	16.17	-33.35	16.10	12	-9	202	277	0.6	